Water Research 261 (2024) 122023

Contents lists available at ScienceDirect

Water Research

journal homepage: www.elsevier.com/locate/watres

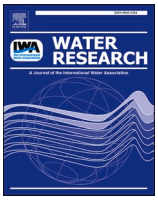

Review

Environmental implications of superoxide radicals: From natural processes to engineering applications

Zonghao Luo [a,b], Yiqi Yan [a,b], Richard Spinney [c], Dionysios D. Dionysiou [d], Frederick A. Villamena [e], Ruiyang Xiao [a,b,*], Davide Vione [f,*]

[a] Institute of Environmental Engineering, School of Metallurgy and Environment, Central South University, Changsha, 410083, China
[b] Chinese National Engineering Research Center for Control & Treatment of Heavy Metal Pollution, Changsha, 410083, China
[c] Department of Chemistry and Biochemistry, The Ohio State University, Columbus, Ohio, 43210, USA
[d] Environmental Engineering and Science Program, University of Cincinnati, Cincinnati, Ohio, 45221, USA
[e] Department of Biological Chemistry and Pharmacology, The Ohio State University, Columbus, Ohio, 43210, USA
[f] Department of Chemistry, University of Turin, Via Pietro Giuria 5, 10125, Torino, Italy

ARTICLE INFO

Keywords:
Superoxide radical
Aquatic chemistry
Kinetics
Reactivity
Mechanisms
Environmental implications

ABSTRACT

The roles of superoxide radical ($O_2^{\bullet-}$) in the domains of physiological, physical, and material chemistry are becoming increasingly recognized. Although extensive efforts have been directed to understand $O_2^{\bullet-}$ functions in diverse aquatic systems, there is a lack of systematic and in-depth review for its kinetics and mechanisms in various environmental scenarios. This review aims to bridge this gap through discussion of $O_2^{\bullet-}$ generation pathways under both natural and controlled conditions. The merits and limitations of the generation and detection methods under various conditions are compared, with emphasis on different approaches for the determination of $O_2^{\bullet-}$-triggered reaction kinetics. We summarize the reaction rate constants of $O_2^{\bullet-}$ with organic contaminants covering a wide diversity of structures and reactivity. The comparison indicates that $O_2^{\bullet-}$ exhibits weak reactivity with most contaminants and lacks selectivity towards compounds with different functional groups, except with quinones which exhibit higher reactivity compared to non-quinones. Further, the reaction mechanisms, namely single electron transfer, nucleophilic substitution, hydrogen atom abstraction, and radical-adduct formation, are critically evaluated. Various environmental implications of $O_2^{\bullet-}$ are highlighted including maintenance of biogeochemical iron cycle, synthesis of nanoparticles for antibacterial purposes, desorption of contaminants from heterogeneous interfaces, and synergetic degradation of contaminants.

1. Introduction

Superoxide radical anion ($O_2^{\bullet-}$) is a paramagnetic transient species with both radical and anionic characteristics, and it can be visualized as ground−state dioxygen ($^3\Sigma_g^-O_2$) reduced by one electron (Hayyan et al., 2016). This radical has been a subject of important investigations for many decades in the fields of chemistry, biology, and physiology. Since the $O_2^{\bullet-}$-induced generation of $^{\bullet}OH$ by Haber-Weiss reaction was first proposed in 1932, environmental chemists have gradually recognized $O_2^{\bullet-}$ as an environmentally significant molecule (Fenton, 1894; Koppenol, 2001; Lu et al., 2022). Main physicochemical properties of $O_2^{\bullet-}$ have been tabulated (Table 1). The O−O bond length of $O_2^{\bullet-}$ is reported to range from 1.28 to 1.33 Å, which is slightly longer than that of $^3\Sigma_g^-O_2$ (1.21 Å), indicating a 1 ½ bond character with the unpaired electron delocalized between the two oxygen atoms, giving each oxygen atom a charge of -0.5 and 50% spin density distribution (Dietzel et al., 2004). The half-life of $O_2^{\bullet-}$ is thought to be relatively long for a radical, ranging from milliseconds to seconds in aqueous solutions, whereas other reactive oxygen radical species such as hydroxyl radical ($^{\bullet}OH$) and sulfate radical ($SO_4^{\bullet-}$) have shorter half-lives (on the scale of nanosecond and microsecond, respectively) (Bielski et al., 1985; Medinas et al., 2007). As a rather strong Brønsted-Lowry base, $O_2^{\bullet-}$ is protonated to its conjugate acid, hydroperoxyl radical ($HO_2^{\bullet}$, $pK_a = 4.8$), in acidic solutions:(Bielski et al., 1985)

$$O_2^{\bullet-} + H^+ \rightleftarrows HO_2^{\bullet} \quad (1)$$

The most characteristic feature of $O_2^{\bullet-}$ includes self−disproportionation and catalytic disproportionation reactions (Ma et al., 2019). Self−disproportionation (or with its conjugate acid) occurs

* Corresponding authors.
E-mail addresses: xiao.53@csu.edu.cn (R. Xiao), davide.vione@unito.it (D. Vione).

https://doi.org/10.1016/j.watres.2024.122023
Received 29 May 2024; Received in revised form 27 June 2024; Accepted 28 June 2024
Available online 1 July 2024

Nomenclatures and abbreviations

chemicals

Adr	adrenaline
AgNPs	silver nanosized particles
BQ	*p*-benzoquinone
BaP	benzo[a]pyrene
BMPO	5-tert-butoxycarbonyl-5-methyl-1-pyrroline-N-oxide
DOM	dissolved organic matter
CDOM	chromophoric dissolved organic matter
DO	dissolved oxygen
^{1}CDOM*	singlet excited state CDOM
^{3}CDOM*	triplet excited state CDOM
DTBQ	3,5-di-*tert*-butylquinone
DNAPL	dense non-aqueous phase liquid
DMPO	5,5-dimethyl-1-pyrroline-n-oxide
DMSO	dimethyl sulfoxide
DMF	N,N-dimethylformamide
DEPMPO	5-diethoxyphosphoryl-5-methyl-1-pyrroline-N-oxide
DF	bis(2,4-dinitrobenzenesulfonyl) fluoresceins
eNOS	endothelial NO synthase
EDTA	ethylenediaminetetraacetic acid
FVH	flavonoids
HPX	hypoxanthine
H4B	tetrahydrobiopterin
IPA	isopropanol
MF	mono formazan
NADPH	nicotinamide adenine dinucleotide phosphate
MCLA	methylcypridina luciferin analog
MC−LR	microcystin−LR
NBT^{2+}	nitro-blue tetrazolium
NaPCP	sodium pentachlorophenate
PFCA	perfluorocarboxylic acid
PFOA	perfluorooctanoic acid
ROS	reactive oxygen species
SRFA	Suwannee river fulvic acid
SOD	superoxide dismutase
TNM	tetranitromethane
TAM	triarylmethyl radical
UA	uric acid
XOD	xanthine oxidase
XAN	xanthine

others

A	$O_2^{\bullet-}$ scavenging activity
ANN	artificial neural network
CV	cyclic voltammetry
DFT	density functional theory
FNSA	fractional negatively charged partial surface area
HOMO	highest occupied molecular orbital
QSAR	quantitative structure-activity relationship
ESR	electron spin resonance
EPR	electron paramagnetic resonance
F	formation rate of $O_2^{\bullet-}$
HAA	hydrogen atom abstraction
ISC	intersystem crossing
ISCO	*in situ* chemical oxidation
KIE	kinetic isotope effects
k	second-order reaction rate constant
k_d	diffusion-controlled rate constant
S_N2	bimolecular nucleophilic substitution
k_D	self-disproportionation rate constant
k_{TC}	rate constant between $O_2^{\bullet-}$ and TC
k_{RC}	rate constant between $O_2^{\bullet-}$ and RC
NHE	normal hydrogen electrode
p.b.k.	product buildup kinetics
pK_a	acid dissociation constant
LUMO	lowest unoccupied molecular orbital
K_d	equilibrium constant for precursor complex formation
R	ratio of $O_2^{\bullet-}$ consumption by the TC
RC	reference compound
RAF	radical adduct formation
SCE	standard calomel electrode
SET	single electron transfer
k'	first-order reaction rate constant
SOLU	solubility
TC	target compound
v_w	formation rate of $RC^{\bullet-}$ with TC
$v_{w/o}$	formation rate of $RC^{\bullet-}$ without TC
A_w	change of absorbance with TC
$A_{w/o}$	change of absorbance without TC
ΔH	hydration enthalpy
Z	universal collision frequency factor

as follows (Rose and Waite, 2005):

$$2O_2^{\bullet-} + H_2O \rightarrow {}^1O_2 + HO_2^- + OH^- \quad (2)$$

$$HO_2^{\bullet} + O_2^{\bullet-} \rightarrow {}^1O_2 + HO_2^- \quad (3)$$

Fig. 1 illustrates the self-disproportionation rate constant (k_D), which gradually increases with pH until 4.8 and then decreases linearly with the increase in pH (Bielski and Allen, 1977). At environmentally relevant pH (~7), the k_D value of $O_2^{\bullet-}$ is approximately 5×10^5 M^{-1} s^{-1}, indicating an important sink for $O_2^{\bullet-}$ in natural waters. Catalytic disproportionation reaction of $O_2^{\bullet-}$ can be initiated by geochemical metals (M) such as Fe, Mn, and Cu species (Fujii et al., 2008; Hansard et al., 2011; Voelker et al., 2000):

$$M^{(n+1)+} + O_2^{\bullet-} \rightarrow M^{n+} + O_2 \quad (4)$$

$$M^{n+} + O_2^{\bullet-} \xrightarrow{2H^+} M^{(n+1)+} + H_2O_2 \quad (5)$$

Metal ions can catalyze the disproportionation of $O_2^{\bullet-}$, and this pathway contributes to about 80% of $O_2^{\bullet-}$ decay (Wuttig et al., 2013a). In addition, dissolved organic matter (DOM), ubiquitous component in various waters, also catalyzes the disproportionation of $O_2^{\bullet-}$ with a rate constant of 2×10^3 $(mg_C/L)^{-1}$ s^{-1}, acting as another $O_2^{\bullet-}$ sink (Fujii and Otani, 2017).

$$O_2^{\bullet-} + DOM \rightarrow O_2 + DOM^{\bullet-} \quad (6)$$

$$O_2^{\bullet-} + DOM^{\bullet-} \xrightarrow{2H^+} H_2O_2 + DOM \quad (7)$$

Specifically, $O_2^{\bullet-}$ reacts with many moieties in DOM molecules, such as quinone, hydroquinone, and semiquinone to produce $DOM^{\bullet-}$ (Eq. 6) (Sheng et al., 2014). Further, $DOM^{\bullet-}$ reacts with $O_2^{\bullet-}$ forming H_2O_2 and DOM (Eq. 7), accounting for the catalytic role of DOM in the disproportionation of $O_2^{\bullet-}$.

Increasing knowledge about $O_2^{\bullet-}$ has considerably promoted related research in the field of environmental science and technology. $O_2^{\bullet-}$ can induce the production of $^{\bullet}OH$ in the presence of iron species and humic DOM. The production of $^{\bullet}OH$ induced by $O_2^{\bullet-}$ and DOM exceeds the stoichiometry of Fenton's reaction by about 24 fold, and $^{\bullet}OH$ then efficiently eliminates anthropogenic contaminants in natural aquatic

Table 1
Physicochemical properties of $O_2^{\bullet-}$.

property	value	reference
O−O bond distance	1.28 Å	(Hayyan et al., 2016)
absorption maximum	240 nm	(Bielski et al., 1985)
extinction coefficient	2350 ± 120 $M^{-1}cm^{-1}$	(Jones et al., 2011)
charge	−1	/
radius	4.32 Å	calculated
diffusion coefficient in water	1.5×10^{-5} cm^2 s^{-1}	(Bielski et al., 1985)
reduction potential in water	−0.33 V	(Ilan et al., 1974; Wood, 1974)
pK_a	4.8	(Bielski, 1978)
electron affinity	0.45 (±0.006) eV	(Ervin et al., 2003)
ΔH (hydration enthalpy)	100 kcal mol^{-1}	(Sawyer, 1991)
dissociation energy	3.1 (±0.4) eV	(Partridge et al., 1992)
half-life	from s to min	(Sutherland et al., 2020)

systems (Xiao et al., 2020). In addition, $O_2^{\bullet-}$, as a strong nucleophile (especially in nonpolar environments), can quickly degrade dense non−aqueous phase liquid (DNAPL) contaminants, which are difficult to degrade by commonly-seen reactive oxygen species (ROS) in advanced oxidation processes (*e.g.,* $^{\bullet}OH$) (Teel and Watts, 2002). Instead of $^{\bullet}OH$, $O_2^{\bullet-}$ was reported to be a responsible species for the degradation of CCl_4 and chloroform in a modified Fenton's system (Watts et al., 1999). Last, $O_2^{\bullet-}$ mediates the redox cycle of Mn(II)/Mn(III) species in seawaters, maintaining normal photosynthesis levels in marine plants (Wuttig et al., 2013b). To quantify the process, the reaction of trace level Mn(II) with $O_2^{\bullet-}$ was monitored by the chemiluminescence method (Hansard et al., 2011). The observed $O_2^{\bullet-}$ decay kinetics strongly suggested that a fast redox cycle of dissolved Mn(II)/Mn(III) occurred in the presence of a continuous source of $O_2^{\bullet-}$, ensuring a significant concentration of Mn(III) in seawaters.

Although many studies made pioneering and significant contributions to our understanding of superoxide chemistry, up-to-date systematic review concerning its environmental implications is still lacking. Within this context, this critical review aims to provide a comprehensive view into the knowledge of $O_2^{\bullet-}$. We first review the approaches for the determination of $O_2^{\bullet-}$-triggered reaction kinetics, and mechanisms for the reactions of $O_2^{\bullet-}$ with anthropogenic contaminants. Then, the computational chemistry and quantitative structure−activity relationship (QSAR) models for prediction of $O_2^{\bullet-}$ reactivity are also discussed. We collected $O_2^{\bullet-}$ kinetic data from 1985 onward (Bielski *et al.* compiled kinetic data for the reactions of $O_2^{\bullet-}$ with more than 300 chemicals in 1985) (Bielski et al., 1985). Finally, we highlight the environmental implications of $O_2^{\bullet-}$, including transformation of metals in natural waters, synthesis of nanoparticles for antibacterial purposes, desorption of contaminants from heterogeneous interfaces, and synergetic degradation of contaminants. We aim to present opportunities for innovation allowing us to transition beyond the current state-of-the-art on $O_2^{\bullet-}$.

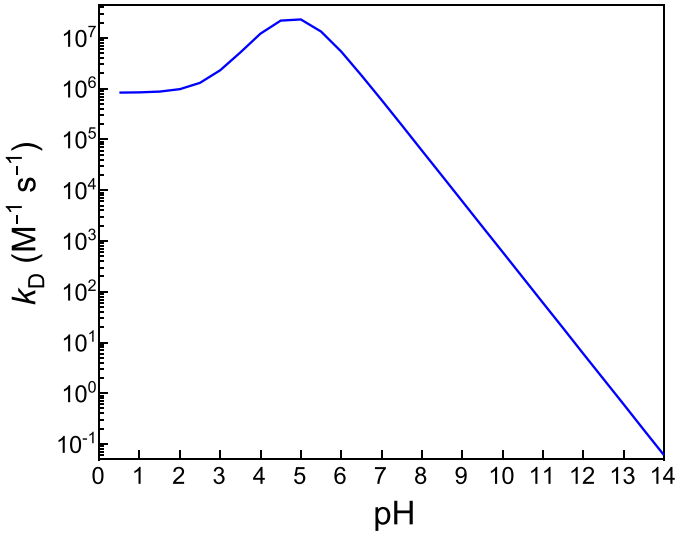

Fig. 1. Observed disproportionation rate constant (k_D) for the decay of $O_2^{\bullet-}$ plotted as a function of pH.

2. Reaction kinetics and mechanisms

The rate constants (k) for bimolecular reactions involving $O_2^{\bullet-}$ and

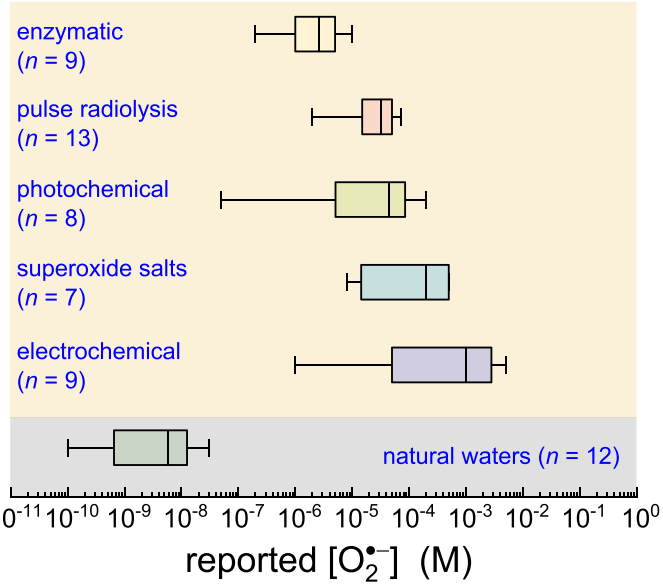

Fig. 2. Comparison of the concentration of $O_2^{\bullet-}$ in controlled (yellow shadow) and natural (grey shadow) systems. (The vertical black lines of each box plot represent (from left to right) minimum, lower-quartile, median, upper-quartile and maximum values.) (Beauchamp and Fridovich, 1971; Berger et al., 2011; Bielski and Arudi, 1983; Brigelius et al., 1974; Burns et al., 2012; Chern et al., 1978; Chin et al., 1982; Divišek and Kastening, 1975; Durot et al., 2005; Felix et al., 1993; Fielden et al., 1974; Fujita et al., 2009; Garg et al., 2011; Georgiou et al., 2015; Goldstein and Czapski, 1990; Goldstein et al., 1990; Goldstone and Voelker, 2000; Grivennikova and Vinogradov, 2006; Hansard et al., 2011; Hansard et al., 2010; Holroyd and Bielski, 1978; Jones et al., 2011; Joshi, 2017; Kelley et al., 2010; Kettle et al., 1988; Klug-Roth et al., 1973; Klug et al., 1972; Kobayashi et al., 1989; Kobayashi et al., 1995; Liang et al., 2019; Liou and Dodd, 2021; Liu et al., 2015; Lokesh and Cunningham, 1986; Luo et al., 2021b; Ma et al., 2020; Marklund, 1976; McDowell et al., 1983; Mesároš et al., 1998; Muhammad et al., 2018; Olean-Oliveira et al., 2019; Peover and White, 1966; Petasne and Zika, 1987; Privat et al., 1997; Rose and Waite, 2006; Rotilio et al., 1972; Rush et al., 1996; Sawyer and Roberts, 1966; Shaked et al., 2010; Stoin et al., 2013; Valentine and Curtis, 1975; Voelker et al., 2000; Wang et al., 2017; Wang et al., 2018a; Wei et al., 2004; Wei et al., 2003; Yeager, 1984; Zafiriou, 1990; Zhang et al., 2017).

target compounds (TCs) can be determined using direct or indirect approaches. The determination of k value by direct methods includes monitoring the decay of $O_2^{\bullet-}$ and the formation kinetics of product(s), whereas indirect methods are employed using a reference compound competing with the target compound (TC) for $O_2^{\bullet-}$. We here summarize the k values of compounds with environmental relevance, and evaluate the impacts of chemical structures of TC on their reactivity towards $O_2^{\bullet-}$. We also describe models that could predict k values with high throughput at the screening level. The $O_2^{\bullet-}$ generation methods under both natural and controlled conditions are discussed (Text S1 in Supplementary Materials), and the concentration of $O_2^{\bullet-}$ in these systems is illustrated in Fig. 2. The advantages and disadvantages of generation and detection methods are compared (Table 2 and 3). This discussion and summary aim to provide better guidance to choose a method with high specificity and suitability.

2.1. Reaction kinetics

2.1.1. Direct methods

2.1.1.1. Decay of $O_2^{\bullet-}$. Many chemical approaches can be applied to monitor the decay of $O_2^{\bullet-}$, however methods such as CV and ESR are more easily subjected to interference from coexisting species. Here, we only introduce the spectrophotometric method, as it has advantages over other methods in simplicity and specificity (Waddell, 1956). In the absence of the TC, the decay of $O_2^{\bullet-}$ due to disproportionation follows a second–order kinetics (Ma et al., 2019):

$$-\frac{d[O_2^{\bullet-}]}{dt} = 2k_D[O_2^{\bullet-}]^2 \quad (8)$$

The k_D value is here determined by fitting the decay curve of $O_2^{\bullet-}$ at certain pH (Fig. 1). While in the presence of TC, the decay of $O_2^{\bullet-}$ was attributed to disproportionation of $O_2^{\bullet-}$ and reaction of $O_2^{\bullet-}$ with TC. Thus, the k value between $O_2^{\bullet-}$ and TC can be determined (Heller and Croot, 2010):

$$-\frac{d[O_2^{\bullet-}]}{dt} = 2k_D[O_2^{\bullet-}]^2 + k'[O_2^{\bullet-}] \quad (9)$$

where k' is the observed decay constant of $O_2^{\bullet-}$ with different concentrations of TC. The k' values can be determined by fitting exponential decay kinetics of $O_2^{\bullet-}$ concentration as function of time. Then, the k value is the slope of the linear fitting between k' and different TC initial concentrations ($k' = k$ [TC]). Our previous study determined the kinetics of $O_2^{\bullet-}$ with a series of perfluorocarboxylic acids (PFCAs) (Bai et al., 2022). The decay rate k' of $O_2^{\bullet-}$ increases with an increasing concentration of PFCAs from 50 μM to 400 μM, and a linear dependence of k' on the various concentrations of PFCAs yields k values ranging from 83.6 M^{-1} s^{-1} to 3.93 × 10^3 M^{-1} s^{-1} (Fig. 3), indicating that the reactivity of $O_2^{\bullet-}$ towards PFCAs is very weak. This method was validated, as PFCAs are unlikely to cause interference due to the absence of UV absorption around 240 nm.

Table 2
Comparison of different methods for the generation of $O_2^{\bullet-}$.

methods	advantages	disadvantages
electrochemical method	a. simple device b. high concentration of $O_2^{\bullet-}$ (millimolar level) c. convenience	a. uneven distribution of $O_2^{\bullet-}$ b. electrode passivation c. coexisting reactive species (*e.g.*, $^{\bullet}OH$ and $^1O_2$)
photochemical method	a. simple device b. high quantum yield	a. coexisting carbon radicals b. organic reagent required (*i.e.*, acetone and ethanol)
chemical reagent method	a. ease of use b. high concentration of $O_2^{\bullet-}$ (millimolar level)	a. byproduct (*e.g.*, KOH) interference b. operational safety
pulse radiolysis method	a. no chemical precursors needed b. no byproduct interference c. high concentration of $O_2^{\bullet-}$ (millimolar level)	a. specialized equipment required b. high level of expertise required
enzymatic method	a. mild $O_2^{\bullet-}$ generation condition b. ease of use (easy to operate and implement) c. relative long (~15 min) steady–state duration	a. byproduct (*e.g.*, uric acid) interference b. narrow working temperature range c. instability of enzyme

Table 3
Comparison of different methods for the detection of $O_2^{\bullet-}$.

methods	advantages	disadvantages
electrochemical method	a. simple device b. *in situ* and real–time detection c. high sensitivity d. low detection limit	a. solution chemistry interference b. specialized equipment needed (*e.g.*, potentiostat)
spectrophotometry	a. *in situ* and real–time detection b. high simplicity and specificity	a. high detection limit b. interference of coexisting species
chemiluminescence method	a. extremely high sensitivity b. *in situ* and real–time detection	a. solution chemistry interference b. use of chemiluminescent chemicals c. lack of selectivity
ESR method	a. fine structural information b. time–resolved measurements c. high specificity	a. specialized equipment needed b. limited selectivity for coexisting species c. use of spin traps

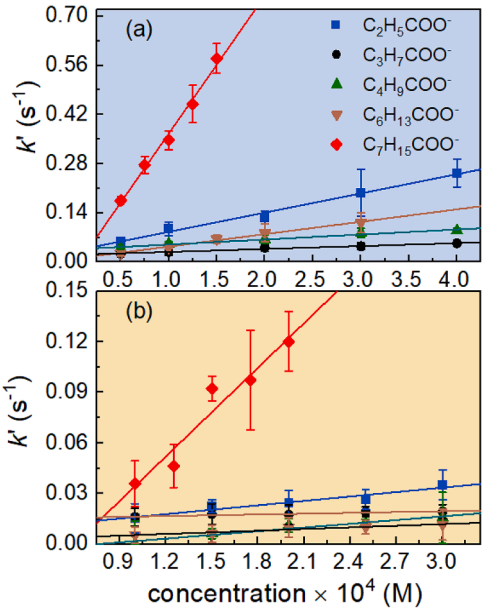

Fig. 3. Observed first–order reaction rate constant (k', s^{-1}) of $O_2^{\bullet-}$ with an increase of PFCA concentrations in aqueous (a) and organic (b) solutions. Error bars represent one standard deviation of the mean ($n \geq 3$). (Reprinted from reference Bai et al. (2022), Copyright 2022 American Chemical Society.)

2.1.1.2. Formation kinetics of product. The k value between TC and $O_2^{\bullet-}$ can also be measured by following the time–dependent absorption of product (product buildup kinetics, p.b.k.) (Greenstock and Ruddock, 1976). This technique requires the product of the reaction to have a decent UV absorption far away from that of $O_2^{\bullet-}$ (240 nm). As an

alternative, the concentration of the product should rapidly reach values that are much higher than $[O_2^{\bullet-}]$ (which can occur if the latter is in a steady state), in which case the absorbance of $O_2^{\bullet-}$ would be negligible. In the presence of TC, the formation kinetics of the product at its characteristic absorption feature can be expressed by (Ma et al., 2021):

$$\frac{d[product]}{dt} = k[O_2^{\bullet-}][TC] \quad (10)$$

When TC is in excess as compared to $O_2^{\bullet-}$ and its reactivity is high, the disproportionation can be neglected, and the formation of product can be written as:

$$[product]_t = [O_2^{\bullet-}]_0 - [O_2^{\bullet-}]_t = [O_2^{\bullet-}]_0 - [O_2^{\bullet-}]_0 e^{k't} \quad (11)$$

where k' is the observed formation rate of product. Then, k can be obtained at different values of $[TC]_0$:

$$k' = k[TC]_0 \quad (12)$$

The p.b.k. technique has been successfully applied to measure the k value between $O_2^{\bullet-}$ and *p*–benzoquinone (BQ) in a pulse radiolysis system (Greenstock and Ruddock, 1976). The formation rate of the product of BQ increases with an increased concentration of BQ, and the k value was derived to be 9×10^8 M^{-1} s^{-1} (Fig. 4). The success of this study was attributed to the product of the reaction exhibiting a characteristic absorption peak at 410 nm. In the direct method, particularly when measuring the formation kinetics of products, a limitation is that the reaction products are often transient species, especially in electron transfer reactions. When quantifying these species, it is crucial to account for their simultaneous decay. In addition, the formation of a product from the reaction of $O_2^{\bullet-}$ with TC may involve multiple steps. Therefore, product formation kinetics may not accurately reflect the reaction rate of $O_2^{\bullet-}$, potentially leading to measurement errors.

2.1.2. Indirect methods

2.1.2.1. Formation kinetics of product of RC. The k value can be determined by monitoring the formation rate of product of RC by competition kinetics technique in an $O_2^{\bullet-}$ steady-state system (Pasternack and Halliwell, 1979). The successful implementation of this method depends on the continuous generation of stable products. The generated $O_2^{\bullet-}$ in the system reacts with both TC and RC:

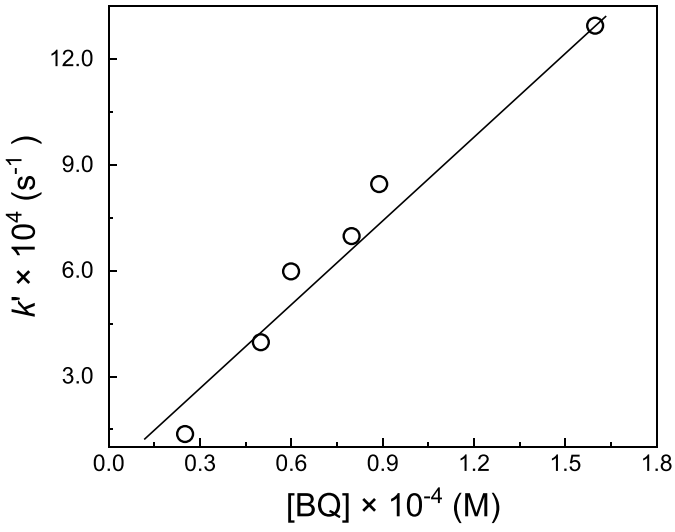

Fig. 4. Observed first–order formation rate of $BQ^{\bullet-}$ as a function of different BQ concentrations. (This Fig. is reproduced from Fig. 1 in reference Greenstock and Ruddock (1976), Copyright 1976 Elsevier.)

$$TC + O_2^{\bullet-} \xrightarrow{k_{TC}} TC^{\bullet-} + O_2 \quad (13)$$

$$RC + O_2^{\bullet-} \xrightarrow{k_{RC}} RC^{\bullet-} + O_2 \quad (14)$$

where k_{TC} and k_{RC} are the second-order k values for the reaction of $O_2^{\bullet-}$ with TC and RC, respectively. Tetranitromethane (TNM) and NBT^{2+} are the frequently used RCs. The reaction of TNM and NBT^{2+} with $O_2^{\bullet-}$ yields stable–colored products nitroform and formazan, and their concentrations can be conveniently measured using a UV spectrophotometer at 350 nm and 560 nm, respectively. In addition, their reaction kinetics with $O_2^{\bullet-}$ are well documented with k values of TNM and NBT^{2+} of 2×10^9 M^{-1} s^{-1} and 6×10^4 M^{-1} s^{-1}, respectively (Guo et al., 2021a). Thus, the k value of $O_2^{\bullet-}$ reacting with TC can be determined by comparing the formation rate of $RC^{\bullet-}$ in the presence and absence of TC. In the presence of TC and RC, the decay of $O_2^{\bullet-}$ can be described:

$$\frac{d[O_2^{\bullet-}]}{dt} = F - k_{TC}[TC][O_2^{\bullet-}] - k_{RC}[RC][O_2^{\bullet-}] = 0 \quad (15)$$

where F is the formation rate (M s^{-1}) of $O_2^{\bullet-}$ in the system. In the presence of TC, the formation rate (v_w, M s^{-1}) of $RC^{\bullet-}$ can be expressed as:

$$v_w = \frac{d[RC^{\bullet-}]}{dt} = k_{RC}[RC][O_2^{\bullet-}] \quad (16)$$

By rearranging Eq. (15), $[O_2^{\bullet-}]$ can be given as:

$$[O_2^{\bullet-}] = \frac{F}{k_{TC}[TC] + k_{RC}[RC]} \quad (17)$$

By substituting Eq. (17) into (16), Eq. (16) can be expressed as:

$$v_w = \frac{d[RC^{\bullet-}]}{dt} = \frac{F\, k_{RC}[RC]}{k_{TC}[TC] + k_{RC}[RC]} \quad (18)$$

In the absence of TC and with $O_2^{\bullet-}$ in a steady state, Eq. (15) is modified as follows:

$$\frac{d[O_2^{\bullet-}]}{dt} = F - k_{RC}[RC][O_2^{\bullet-}] = 0 \quad (19)$$

Thus, the formation rate ($v_{w/o}$) of $RC^{\bullet-}$ is given as:

$$v_{w/o} = \frac{d[RC^{\bullet-}]}{dt} = k_{RC}[RC][O_2^{\bullet-}] \quad (20)$$

Finally, by substituting Eq. (19) into Eq. (20), and further comparing with Eq. (18), one could obtain:

$$\frac{v_{w/o}}{v_w} = \frac{k_{TC}[TC]}{k_{RC}[RC]} + 1 \quad (21)$$

This method was used to investigate the kinetics between $O_2^{\bullet-}$ and iron complex by the formation kinetics of the RC product (in such case RC was NBT^{2+}). The formation of products showed a linear relationship as function of time, and the k values of $O_2^{\bullet-}$ with Fe $(EDTA)^{2-}$ and Fe $(EDTA)^{-}$ were measured to be 3×10^5 and 2×10^5 M^{-1} s^{-1}, respectively (Fig. 5) (Pasternack and Halliwell, 1979). It should be noted that the k values of $O_2^{\bullet-}$ with TCs and RCs are expected to be within 1 order of magnitude for the application of the competition technique (Yu, 2004).

2.1.2.2. Formation quantity of product of RC. Instead of formation rate, the k value for the reaction of $O_2^{\bullet-}$ with TC can be also measured based on formation quantity of product of RC using adrenaline (Adr) (Bors et al., 1978). The product (*i.e.*, $AdrO^{\bullet}$) of Adr reacting with $O_2^{\bullet-}$ has a characteristic absorption at 485 nm:

$$O_2^{\bullet-} + Adr \rightarrow AdrO^{\bullet} + H_2O_2 \quad (22)$$

The k value between TC and $O_2^{\bullet-}$ can be determined from the change

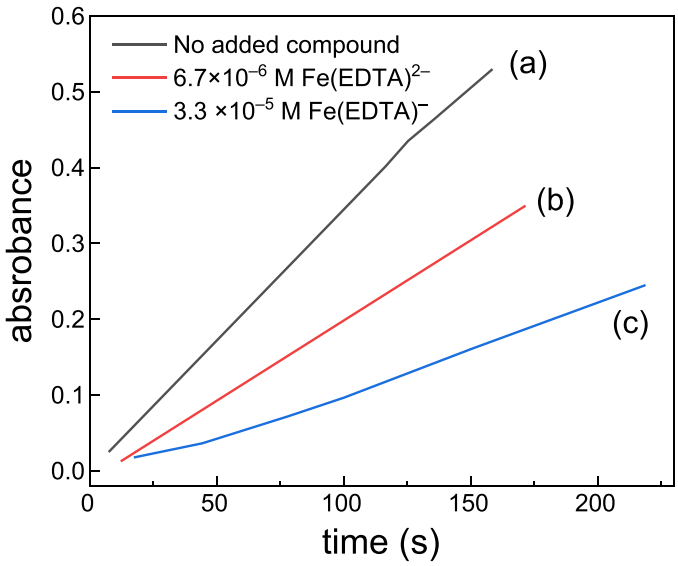

Fig. 5. Effect of iron complexes on reduction of NBT^{2+} by $O_2^{\bullet-}$ at pH 10.1. (a): no added compound. (b): Assay mixture to which 6.7×10^{-6} M $Fe(EDTA)^{2-}$ has been added. (c) Assay mixture to which 3.3×10^{-5} M $Fe(EDTA)^{-}$ has been added. (This Fig. is reproduced from Fig. 1 in reference Pasternack and Halliwell (1979), Copyright 1979 American Chemical Society.)

of absorbance after a definite reaction time under different concentrations of TC:

$$\frac{A_{w/o}}{A_w} = 1 + \frac{k \times [TC]}{k_{Adr} \times [Adr]} \quad (23)$$

where k_{Adr} is the rate constant of Eq. (22) (2.5×10^4 M^{-1} s^{-1}), $A_{w/o}$ and A_w are the changes in absorbance without and with TC. With this technique, the k value between $O_2^{\bullet-}$ and sulfacetamide (SCT) was measured to be 45 M^{-1} s^{-1} (Fig. 6) (Luo et al., 2021a). This method also suffers from limitations. AdrO$^{\bullet}$ is only stable to a limited extent due to its radical nature, and it will decay in a short period of time. Thus, the measurement should be conducted within a few minutes.

2.1.2.3. Method of 50% inhibition. The reaction kinetics of $O_2^{\bullet-}$ with TCs can be also determined by ESR. It is reported that DMPO can react with $O_2^{\bullet-}$ stoichiometrically (1:1) to yield DMPO–$O_2^{\bullet-}$ (Sawada and Yamazaki, 1973). This stoichiometric relationship allows for the determination of kinetics between $O_2^{\bullet-}$ and other TCs by competitive technique. When other $O_2^{\bullet-}$ scavengers (*e.g.,* L-ascorbic acid, catalase, and ceruloplasmin) were introduced, they could react with $O_2^{\bullet-}$, thus hindering the formation of DMPO–$O_2^{\bullet-}$ (Mitsuta et al., 1990). As the formation signal of DMPO–$O_2^{\bullet-}$ decreases by 50%, the ratio of k_{TC} to k_{DMPO} is equal to the ratio of [DMPO] to [TC]. Therefore, the k value between $O_2^{\bullet-}$ and various TCs can be determined. The formation rates of DMPO–$O_2^{\bullet-}$ and TC–$O_2^{\bullet-}$ are given by, respectively:

$$\frac{d[DMPO - O_2^{\bullet-}]}{dt} = k_{DMPO}[DMPO][O_2^{\bullet-}] \quad (24)$$

$$\frac{d[TC - O_2^{\bullet-}]}{dt} = k_{TC}[TC][O_2^{\bullet-}] \quad (25)$$

Dividing Eq. (25) by Eq. (24), the formation rate can be expressed by:

$$\frac{d[DPMO - O_2^{\bullet-}]}{dt} : \frac{d[TC - O_2^{\bullet-}]}{dt} = (1 - R) : R \quad (26)$$

where R is the ratio of $O_2^{\bullet-}$ consumption by the TC. From the above equations, the following equation can be derived:

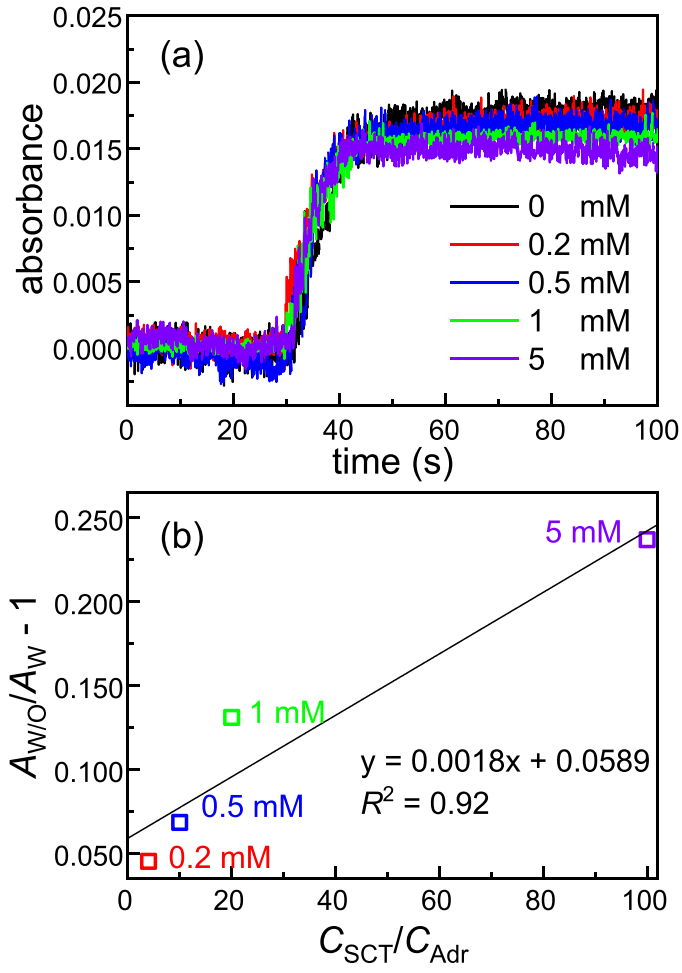

Fig. 6. (a) Evolution of the absorbance (A) in working solutions containing target compound sulfacetamide (SCT) and competitor Adr ([SCT] = 0–5 mM, [Adr] = 50 μM, and pH 8). (b) $A_{W/O}/A_W - 1$ of the working solutions as a function of C_{SCT}/C_{Adr}. (Reprinted from reference Luo et al. (2021a), Copyright 2021 American Chemical Society.)

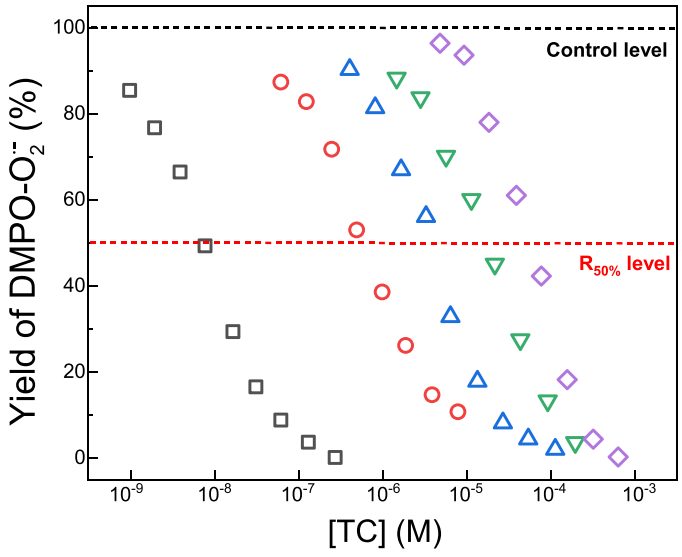

Fig. 7. The relationship between the signal intensities of DMPO–$O_2^{\bullet-}$ and the concentration of various TCs (Fe–SOD (□), peroxidase (○), ascorbate oxidase (△), catalase (▽), ascorbic acid (◇)). (This Fig. is reproduced from Fig. 1 in reference Mitsuta et al. (1990), Copyright 1990 Chemical Society of Japan)

$$k_{TC} = k_{DMPO} \times \frac{R}{1-R} \times \frac{[DMPO]}{[TC]} \quad (27)$$

In the case of 50% inhibition ($R = 50\%$), Eq. (27) can be simplified to:

$$k_{TC} = k_{DMPO} \frac{[DMPO]}{R_{50\%}} \quad (28)$$

In the above equation, $R_{50\%}$ is the experimental concentration of TC at 50% inhibition. As shown in Fig. 7, the reactivity of $O_2^{\bullet-}$ towards five compounds in an HPX/XOD enzymatic system has been investigated with batch experiments (Mitsuta et al., 1990). The k values were measured by means of 50% inhibition, and the inhibitory effect occurred in the order: Fe–SOD (2.4×10^9 M^{-1} s^{-1}) > peroxidase (2.4×10^7 M^{-1} s^{-1}) > ascorbate oxidase (4.8×10^6 M^{-1} s^{-1}) > catalase (9.6×10^5 M^{-1} s^{-1}) > ascorbic acid (3.5×10^5 M^{-1} s^{-1}). However, the use of this method was plagued by many limitations. First, it requires a large-scale concentration gradient of TC to ensure the accuracy of the determined k value, which is challenging to achieve for poorly water–soluble compounds. In addition, the method of 50% inhibition used in the enzymatic systems can also produce $^{\bullet}OH$, which reacts with DMPO to form other adducts. This side reaction may interfere with the reaction of TC with $O_2^{\bullet-}$, resulting in lower accuracy. Further, many studies pointed out that great care should be exerted with competition methods for kinetic investigations (this is particularly true for determining the k value, when k is derived from the formation of multi-step reaction products rather than the daughter product) (Bielski and Cabelli, 1991)

In an indirect method, the reaction product of $O_2^{\bullet-}$ with RC may react with TC, leading to error propagation for the k value of $O_2^{\bullet-}$ and TC. In addition, measurement errors can arise in multi-radical systems due to the difficulty in determining the contribution of the target radical.

2.1.3. QSAR model

Recognizing that thousands of contaminants have been emitted to the environment, experimental determination of the $O_2^{\bullet-}$–mediated oxidation kinetics is cost–intensive and time–consuming. To fill the gap between limited experimental data and increasing numbers of TCs, computational tools such as QSAR models and artificial neural network (ANN) methods, have been utilized (Xiao et al., 2015; Ye et al., 2017). In QSAR modeling, a statistical analysis is employed to establish mathematical relationships between molecular descriptors and reactivity of selected compounds with $O_2^{\bullet-}$. The established relationship can then be applied to predict TC with unknown k values.

A QSAR model was developed to predict the ability of chalcones to scavenge $O_2^{\bullet-}$ (Sivakumar et al., 2011). It was determined based on the ability of chalcones to inhibit the reduction of NBT^{2+}. The Cerius^2 software was used to develop the descriptors of chalcones, and the data was analyzed by statistical regression using Kyplot software. Topological, thermodynamic, and spatial descriptors were calculated on the basis of the optimized structures of chalcones, and then the developed QSAR model (Eq. (29)) was subjected to external and internal validations (Yamagami et al., 2005).

$$A = 1.0898 - 7.6121 \times FNSA + 0.4929 \times SOLU \quad (29)$$

where A is the $O_2^{\bullet-}$ scavenging activity (unitless), FNSA is known as fractional negatively charged partial surface area, and SOLU is the aqueous solubility of chalcones (Bednarczyk et al., 2003). With r^2 and q^2 values greater than 0.6 and 0.5, respectively, it was concluded that the QSAR model could efficiently predict the scavenging ability of different chalcones towards $O_2^{\bullet-}$. However, there are a few limitations to the application of this model. The model was built based on the aqueous solubility of chalcone derivatives, but this descriptor is expected to exhibit very limited effects on chemical reactions. In addition, the developed model only reflects an empirical numerical relationship between A and the other two parameters, and the mathematical combination of FNSA and SOLU does not seem to make any mechanistic sense.

A more generic QSAR model was then developed by Nolte and Peijnenburg (2018). This model was able to predict k values across various chemical classes. The k values were collected *via* Web of Science and the National Diagnostic Reference Level/National Institute of Standards and Technology Solution Kinetics Database (NIST, 2002). The final dataset contained 238 TCs with a wide range of reactivities and structures. The structures were optimized, and quantum chemical molecular descriptors such as, E_{HOMO}, E_{LUMO}, polarizability and dipole moment, were calculated by semi-empirical quantum chemical method PM7 (Stewart, 2013). Stepwise regression was used to select descriptors and develop the QSAR model. Finally, a reductive model was developed for $O_2^{\bullet-}$ (pH > 7), and an oxidative model for $HO_2^{\bullet}$ (pH < 4.9):

$$\log k_{O_2^{\bullet-}} = -2.5 \times E_{LUMO} + 3.2 \quad (30)$$

$$\log k_{HO_2^{\bullet}} = 2.1 \times E_{HOMO} + 22.9 \quad (31)$$

For both models, R^2 values were greater than 0.8, indicating an excellent predictivity and robustness. These models should not be applied to radical intermediates, stabilized radicals, and metal–containing complexes. However, a few limitations remain to be considered. The data utilized in the mentioned research is derived from different methods, thereby potentially introducing uncertainty. In addition, the developed QSAR model exhibited a narrow applicability domain due to the complex reactivity and limited kinetic data for $O_2^{\bullet-}$. To overcome these limitations, it is essential to develop more reliable experimental determination methods to ensure the accuracy of data used for model training. Further, incorporating the quantification of uncertainty from kinetic data into QSAR and ANN predictions is necessary to enhance the reliability of model outputs and performance assessments. The robustness of QSAR models depends on the quality of the data for training models (this could be an inherent issue for any QSAR model). For example, Land et al. (2010) measured the k value between $O_2^{\bullet-}$ and sulfacetamide to be 7×10^7 M^{-1} s^{-1} by laser flash photolysis, but another experimental study determined this value to be extremely small (at least 3 orders of magnitude lower) using three discrete techniques, namely spectrophotometry, chemiluminescence, and theoretical calculation (Luo et al., 2021a).

2.1.4. Comparison of reactivity

Bimolecular reaction rate constants (k, M^{-1} s^{-1}) are of particular importance for understanding the reaction mechanisms and reactivity of $O_2^{\bullet-}$ with various TCs. Table 4 tabulates k values for $O_2^{\bullet-}$-induced reactions from 1985 onward, as there exists an excellent k data compilation by Bielski *et al.* in that year (Bielski et al., 1985). Among the collected TCs, aromatic hydrocarbon derivatives, heterocycles, and halogenated alkane compounds account for the large majority. The methods for determination of k values are also listed in the table, and we grouped them into the direct (blue shadowed part) and indirect (green shadowed part) methods (Table 4). The k values of $O_2^{\bullet-}$ reacting with TCs range from 10 M^{-1} s^{-1} to 2.3×10^9 M^{-1} s^{-1}, and the TC with the median k value is quercetin with $k = 4.7 \times 10^4$ M^{-1} s^{-1}. This low median indicates that $O_2^{\bullet-}$ typically exhibits at least 3 orders of magnitude smaller rate constants than those of $^{\bullet}OH$ and $SO_4^{\bullet-}$ (usually in the range of 10^7 to 10^9 M^{-1} s^{-1}) (Buxton et al., 1988; Zhang et al., 2015), and the comparative result simply shows that $O_2^{\bullet-}$ exhibits weak reactivity towards most TCs.

The k values of TCs depend on their functional groups. For example, phenol with hydroxyl group exhibits relatively low reactivity ($k = 5.8 \times 10^2$ M^{-1} s^{-1}) towards $O_2^{\bullet-}$, while the k value between $O_2^{\bullet-}$ and p-benzoquinone (quinone group) was reported to be as high as 8.3×10^8 M^{-1} s^{-1}. To explicitly probe the effect of functional groups on the k values in Table 4, the TCs were further classified into different categories, including nitro ($n = 5$), amine ($n = 45$), ether ($n = 14$), carboxyl ($n =$

Table 4
The compilation of rate constants (k, $M^{-1}\ s^{-1}$) for reactions of $O_2^{\bullet-}$ with organic compounds in aqueous solution from 1985 onward. The k values for compounds #1 to #49 were measured using direct methods, whereas compounds #50 to #111 were measured using indirect methods. Square brackets denote concentration (*e.g.*, [TC]: concentration of TC). Abbreviations: AZQ, 2,5-diaziridinyl-3,6-bis(2-hydroxyethylamino)-1,4-benzoquinone; CHDO, 2-spirocyclohexane-5,5-dimethyl-3-oxazolidin-1-oxyl; CMH, 1-hydroxy-3-methoxycarbonyl-2,2,5,5-tetramethylpyrrolidine; Cytc, cytochrome C; ESR, electron spin-resonance; Fecytc, ferricytochrome c; HPX, hypoxanthine; NBT^{2+}, nitro blue tetrazolium; N.R., not reported; OXANO, 2-ethyl-2,5,5-trimethyl-3-oxazolidineoxyl; PCA, 3-carboxamido-2,2,5,5-tetramethylpyrrolidin-1-yloxy; RC, reference compound; SOD, superoxide dismutase; TEMPO, 2,2,6,6-tetramethylpiperidine-n-oxyl; TC, target compound; TNM, tetranitromethane; Tempol, 4-hydroxy-2,2,6,6-tetramethylpiperidine n-oxyl; XAN, xanthine; XOD, xanthine oxidase.

#	compounds	k	pH	methods and reference
1	aniline	5.7×10^1	N.R.	XAN/XOD, decay rates of $O_2^{\bullet-}$ under different [TC]
2	*p*-aminophenol	5.1×10^2	N.R.	XAN/XOD, decay rates of $O_2^{\bullet-}$ under different [TC]
3	aminooxy	2.3×10^7	>11	pulse radiolysis, decay rates of $O_2^{\bullet-}$ under different [TC]
4	AZQ	1.5×10^5	N.R.	pulse radiolysis, decay rates of $O_2^{\bullet-}$ under different [TC]
5	carbon tetrachloride	4.8×10^2	8.0	UV/H_2O_2/formate, decay rates of $O_2^{\bullet-}$ under different [TC]
6	caffeoylputrescine	8.5×10^4	7.5	pulse radiolysis, decay rates of $O_2^{\bullet-}$ under different [TC]
7	acetylated Cytc	1.5×10^5	7.0	pulse radiolysis, decay rates of $O_2^{\bullet-}$ under different [TC]
8	cadaverine	2.9×10^2	7.5	pulse radiolysis, decay rates of $O_2^{\bullet-}$ under different [TC]
9	dihydroethidium	2.2×10^3	7.4	XAN/XOD, fluorescence intensities variations under different [TC]
10	DNA	1.0×10^6	N.R.	pulse radiolysis, decay rates of $O_2^{\bullet-}$ under different [TC]
11	deoxyadenosine monophosphate	1.0×10^6	N.R.	pulse radiolysis, decay rates of $O_2^{\bullet-}$ under different [TC]
12	deoxycytidine monophosphate	1.0×10^6	N.R.	pulse radiolysis, decay rates of $O_2^{\bullet-}$ under different [TC]
13	daunomycin	2.8×10^6	7.0	pulse radiolysis, decay rates of $O_2^{\bullet-}$ under different [TC]
14	ethyl 3,4-dihydroxybenzoate	7.0×10^4	N.R.	pulse radiolysis, absorbance (at 360 nm) of product of the reaction under different [TC]
15	fisetin	1.3×10^4	10	HPX/XOD, ESR intensities variation under different [TC]
16	fluoranil	2.8×10^8	7.0	pulse radiolysis, decay rates of $O_2^{\bullet-}$ under different [TC]
17	galangin	8.8×10^2	10	HPX/XOD, ESR intensities variation under different [TC]
18	hesperidin	2.8×10^4	10	HPX/XOD, ESR intensities variation under different [TC]
19	hesperetin	5.9×10^3	10	HPX/XOD, ESR intensities variation under different [TC]
20	hydroethidine	2.0×10^6	7.4	pulse radiolysis, absorbance (at 472 nm) of product of the reaction under different [TC]
21	3-hydroxykynurenine	1.2×10^5	7.4	pulse radiolysis, decay rates of $O_2^{\bullet-}$ under different [TC]
22	5-hydroxy-1,4-naphthoquinone	1.5×10^8	7.0	pulse radiolysis, decay rates of $O_2^{\bullet-}$ under different [TC]
23	kynurenine	1.2×10^5	7.4	pulse radiolysis, decay rates of $O_2^{\bullet-}$ under different [TC]
24	kaempferol	2.4×10^3	10	HPX/XOD, ESR intensities variation under different [TC]
25	kaempferol	5.5×10^5	7.5	N.R., decay rates of $O_2^{\bullet-}$ under different [TC]
26	methoxatine	2.2×10^8	7.3	pulse radiolysis, decay rates of $O_2^{\bullet-}$ under different [TC]
27	methyl gallate	2.4×10^5	7.0	HPX/XOD, ESR intensities variation under different [TC]
28	morin	1.6×10^3	10	HPX/XOD, ESR intensities variation under different [TC]
29	4-methoxyphenoxide ion	1.8×10^4	10	HPX/XOD, ESR intensities variation under different [TC]
30	N-bromosuccinimide	4.8×10^8	9.3	pulse radiolysis, decay rates of $O_2^{\bullet-}$ under different [TC]
31	OXANO	1.3×10^2	6.5	XAN/XOD, fitted based on removal rates of TC in different steady state of [$O_2^{\bullet-}$]
32	oxyhemoglobin	6.5×10^6	8.5	XAN/XOD, decay rates of $O_2^{\bullet-}$ under different [TC]
33	putrescine	1.1×10^2	7.5	pulse radiolysis, decay rates of $O_2^{\bullet-}$ under different [TC]
34	pentafluoropropionic acid	5.5×10^2	8.0	UV/H_2O_2/formate, decay rates of $O_2^{\bullet-}$ under different [TC]
35	perfluorobutanoic acid	8.4×10^1	8.0	UV/H_2O_2/formate, decay rates of $O_2^{\bullet-}$ under different [TC]
36	perfluoropentaonoic acid	1.4×10^2	8.0	UV/H_2O_2/formate, decay rates of $O_2^{\bullet-}$ under different [TC]
37	perfluoroheptanoic acid	3.5×10^2	8.0	UV/H_2O_2/formate, decay rates of $O_2^{\bullet-}$ under different [TC]
38	perfluorooctanoic acid	3.9×10^3	8.0	UV/H_2O_2/formate, decay rates of $O_2^{\bullet-}$ under different [TC]
39	propyl 3,4,5-trihydroxybenzoate	2.6×10^5	6.8	pulse radiolysis, absorbance (at 440 nm) of product of the reaction under different [TC]
40	6-phosphogluconate dehydratase	2.0×10^8	N.R.	N.R., decay rates of $O_2^{\bullet-}$ under different [TC]
41	quercetin	4.7×10^4	10	HPX/XOD, ESR intensities variation under different [TC]
42	rutin	5.1×10^4	10	HPX/XOD, ESR intensities variation under different [TC]
43	resorcinol	8.0×10^2	N.R.	XAN/XOD, decay rates of $O_2^{\bullet-}$ under different [TC]
44	spermidine	2.9×10^2	7.5	pulse radiolysis, decay rates of $O_2^{\bullet-}$ under different [TC]
45	S-Nitrosoglutathione	3.0×10^2	7.0	pulse radiolysis, absorbance (at 340 nm) of product of the reaction under different [TC]
46	2-tert-butyl-1,4-benzoquinone	1.1×10^8	6.8	pulse radiolysis, formation rates of product of the reaction under different [TC]
47	4′,5,7-trihydroxyflavanone	3.0×10^2	10	HPX/XOD, ESR intensities variation under different [TC]
48	tetrahydroxyquinone	2.0×10^7	7.0	pulse radiolysis, bleaching rates of TC in different steady state of [$O_2^{\bullet-}$]
49	*p*-toluidine	4.0×10^1	N.R.	XAN/XOD, decay rates of $O_2^{\bullet-}$ under different [TC]
50	atrazine	4.1×10^5	8.0	XAN/XOD, absorbance (at 350 nm) of product btw $O_2^{\bullet-}$ and RC (TNM)
51	allopurinol	1.7×10^4	7.4	HPX/XOD, 50% inhibition (see main text)
52	acetaminophen	1.4×10^4	7.4	HPX/XOD, 50% inhibition (see main text)
53	ascorbic acid	3.4×10^5	N.R.	HPX/XOD, 50% inhibition (see main text)
54	2-aminoethanethiol	1.0×10^3	7.4	XAN/XOD, absorbance (at 550 nm) of product btw $O_2^{\bullet-}$ and RC (Cytc)
55	anthraquinone	3.7×10^8	7.4	N.R., N.R.
56	1,4-benzoquinone	8.3×10^8	8.0	XAN/XOD, absorbance (at 350 nm) of product btw $O_2^{\bullet-}$ and RC (TNM)
57	captopril	1.0×10^3	7.4	HPX/XOD, absorbance (at 550 nm) of product btw $O_2^{\bullet-}$ and RC (Cytc)
58	cysteinesulfinic acid	1.0×10^3	7.4	XAN/XOD, absorbance (at 550 nm) of product btw $O_2^{\bullet-}$ and RC (Cytc)
59	coumaric acid	5.5×10^4	7.4	KO_2, chemiluminescence intensities (at 503 nm) of product btw $O_2^{\bullet-}$ and RC (lucigenin)
60	cinnamic acid	5.9×10^3	7.4	KO_2, chemiluminescence intensities (at 503 nm) of product btw $O_2^{\bullet-}$ and RC (lucigenin)
61	catechin	7.1×10^5	7.4	KO_2, chemiluminescence intensities (at 503 nm) of product btw $O_2^{\bullet-}$ and RC (lucigenin)
62	CHDO	3.5×10^2	7.8	HPX/XOD, chemiluminescence intensities (at 503 nm) of product btw $O_2^{\bullet-}$ and RC (lucigenin)
63	3-cyano-proxyl	2.4×10^3	7.8	HPX/XOD, ESR intensities of product btw $O_2^{\bullet-}$ and RC (Fecytc)
64	3-carboxy-proxyl	5.4×10^4	7.8	HPX/XOD, ESR intensities of product btw $O_2^{\bullet-}$ and RC (Fecytc)
65	chloroform	2.3×10^8	8.0	XAN/XOD, absorbance (at 350 nm) of product btw $O_2^{\bullet-}$ and RC (TNM)
66	delphinidin	8.1×10^6	7.4	KO_2, chemiluminescence intensities (at 503 nm) of product btw $O_2^{\bullet-}$ and RC (lucigenin)
67	deethylatrazine	3.1×10^5	8.0	XAN/XOD, absorbance (at 350 nm) of product btw $O_2^{\bullet-}$ and RC (TNM)

(*continued on next page*)

Table 4 (*continued*)

#	compounds	k	pH	methods and reference
68	1,3-dichlorobenzene	7.0×10^7	8.0	XAN/XOD, absorbance (at 350 nm) of product btw $O_2^{\bullet-}$ and RC (TNM)
69	diquat	2.1×10^5	8.0	XAN/XOD, absorbance (at 350 nm) of product btw $O_2^{\bullet-}$ and RC (TNM)
70	epicatechingallate	1.1×10^7	7.4	KO_2, chemiluminescence intensities (at 503 nm) of product btw $O_2^{\bullet-}$ and RC (lucigenin)
71	epicatechin	6.6×10^5	7.4	KO_2, chemiluminescence intensities (at 503 nm) of product btw $O_2^{\bullet-}$ and RC (lucigenin)
72	ergothioneine	1.0×10^3	7.4	HPX-XOD, absorbance (at 550 nm) of product btw $O_2^{\bullet-}$ and RC (Cytc)
73	eugenol	8.3×10^3	N.R.	HPX-XOD, 50 % inhibition (see main text)
74	flurbiprofen	6.5×10^2	7.4	HPX/XOD, 50 % inhibition (see main text)
75	fisetin	7.8×10^5	7.4	KO_2, chemiluminescence intensities (at 503 nm) of product btw $O_2^{\bullet-}$ and RC (lucigenin)
76	furoin	2.5×10^2	6.5	decomposition of H_2O_2, decay rates of TC under different [H_2O_2]
77	glutathione	2.2×10^2	7.4	XAN/XOD, ESR intensities btw $O_2^{\bullet-}$ and spin trap (DMPO)
78	guaiacol	2.5×10^3	N.R.	HPX/XOD, 50% inhibition (see main text)
79	honokiol	3.2×10^5	7.4	XAN/XOD, formation rates of product btw $O_2^{\bullet-}$ and spin trap (CMH)
80	isorhamnetin	7.4×10^4	7.4	KO_2, chemiluminescence intensities (at 503 nm) of product btw $O_2^{\bullet-}$ and RC (lucigenin)
81	ketomalonate dianion	1.5×10^2	10	pulse radiolysis, N.R.
82	kaempferol	2.0×10^4	7.4	KO_2, chemiluminescence intensities (at 503 nm) of product btw $O_2^{\bullet-}$ and RC (lucigenin)
83	leucocyanidol	7.7×10^5	7.4	KO_2, chemiluminescence intensities (at 503 nm) of product btw $O_2^{\bullet-}$ and RC (lucigenin)
84	mitoxantrone	2.0×10^2	7.0	pulse radiolysis, N.R.
85	myricetin	9.0×10^6	7.4	KO_2, chemiluminescence intensities (at 503 nm) of product btw $O_2^{\bullet-}$ and RC (lucigenin)
86	malvidin	6.0×10^5	7.4	KO_2, chemiluminescence intensities (at 503 nm) of product btw $O_2^{\bullet-}$ and RC (lucigenin)
87	naproxen	7.3×10^2	7.4	HPX/XOD, 50% inhibition (see main text)
88	nitecapone	1.0×10^4	8.6	XAN/XOD, absorbance (at 550 nm) of product btw $O_2^{\bullet-}$ and RC (Cytc)
89	nitrosobenzene	4.0×10^5	N.R.	pulse radiolysis, N.R.
90	2-nitropropane	1.0×10^1	7.3	pulse radiolysis, absorbance (at 550 nm) of product btw $O_2^{\bullet-}$ and RC (kaempferol)
91	propane-2-nitronate	7.0×10^2	7.3	pulse radiolysis, absorbance (at 550 nm) of product btw $O_2^{\bullet-}$ and RC (kaempferol)
92	perfluorooctane sulphonate	4.2×10^4	8.0	XAN/XOD, absorbance (at 350 nm) of product btw $O_2^{\bullet-}$ and RC (TNM)
93	perfluorooctanoic acid	6.4×10^7	8.0	XAN/XOD, absorbance (at 350 nm) of product btw $O_2^{\bullet-}$ and RC (TNM)
94	plumbagin	8.9×10^7	7.0	pulse radiolysis, absorbance (at 650 nm) of product btw $O_2^{\bullet-}$ and RC (quinone)
95	PCA	2.0×10^4	7.8	HPX/XOD, ESR intensities of product btw $O_2^{\bullet-}$ and RC (Fecytc)
96	perchlorotriphenylmethyl radical	8.3×10^8	7.4	XAN/XOD, reduction rates of ESR intensities btw $O_2^{\bullet-}$ and RC (SOD)
97	para-chlorobenzoic acid	8.6×10^7	8.0	XAN/XOD, absorbance (at 350 nm) of product btw $O_2^{\bullet-}$ and RC (TNM)
98	phenol	5.8×10^2	N.R.	HPX/XOD, 50% inhibition (see main text)
99	paraquat	1.0×10^4	N.R.	pulse radiolysis, N.R.
100	9,10-phenanthrenequinone	2.3×10^9	7.8	pulse radiolysis, N.R.
101	stobadine	7.5×10^2	7.8	XAN/XOD, chemiluminescence intensities btw $O_2^{\bullet-}$ and RC (SOD)
102	sulfacetamide	4.8×10^1	8.0	UV/H_2O_2/formate, absorbance (at 485 nm) of product btw $O_2^{\bullet-}$ and RC (adrenaline)
103	salicylate	1.2×10^3	7.4	HPX/XOD, 50% inhibition (see main text)
104	triquat	2.4×10^2	N.R.	pulse radiolysis, N.R.
105	Tempol	1.1×10^5	7.8	HPX/XOD, ESR intensities of product btw $O_2^{\bullet-}$ and RC (Fecytc)
106	tempone	4.0×10^4	7.8	HPX/XOD, ESR intensities of product btw $O_2^{\bullet-}$ and RC (Fecytc)
107	trans-resveratrol	6.5×10^3	7.4	KO_2, chemiluminescence intensities (at 503 nm) of product btw $O_2^{\bullet-}$ and RC (lucigenin)
108	tert-nitrosobutane	1.6×10^4	8.2	XAN/XOD, reduction rates of RC (Fecytc) btw $O_2^{\bullet-}$ and spin trap (DMPO)
109	TEMPO	1.2×10^5	7.8	HPX-XOD, chemiluminescence intensities (at 503 nm) of product btw $O_2^{\bullet-}$ and RC (lucigenin)
110	taurine	1.0×10^3	7.4	XAN/XOD, absorbance (at 550 nm) of product btw $O_2^{\bullet-}$ and RC (Cytc)
111	thiourea	1.1×10^3	N.R.	XAN/XOD, reduction rates of RC (Cytc) under different [TC]

15), carbonyl ($n = 45$), hydroxyl ($n = 51$), arene ($n = 72$), alkene ($n = 17$), heteroarene ($n = 20$), and halogen groups ($n = 10$). In Fig. 8a, TCs with different functional groups were sorted by their median of k value. Unlike the trend for $SO_4^{\bullet-}$, for which the k value had a nice linear relationship with the ratio of oxygen atoms to carbon atoms and the energy gap of E_{LUMO} and E_{HOMO} (Wojnárovits and Takács, 2019; Xiao et al., 2015), no obvious trend was observed for TCs with different functional groups. Note that TCs were classified into a subcategory based on the presence of functional groups, thus one compound could be placed into many subcategories.

Mounting evidence has been presented for high reactivity between quinones and $O_2^{\bullet-}$ (Dohrmann and Bergmann, 1995; Mukherjee, 1987). For example, *p*–benzoquinone and 9,10-phenanthrenequinone react with $O_2^{\bullet-}$ showing high k values of 9.8×10^8 and 2.3×10^9 M^{-1} s^{-1}, respectively (Butler and Hoey, 1986; Guo et al., 2021b). Thus, we then classified these TCs into quinones and non-quinones (Fig. 8b). The k values for most quinones range from 10^7 M^{-1} s^{-1} to 10^9 M^{-1} s^{-1}, while the non-quinones range in most cases from 10^2 M^{-1} s^{-1} to 10^6 M^{-1} s^{-1}. Clearly, this discrepancy indicates that $O_2^{\bullet-}$ exhibits strong reactivity towards quinones. It was reported that the fully conjugated cyclic di-one structure gives quinone a redox-active nature, facilitating and accelerating electron transfer from radicals to electron acceptors, thus higher reactivity (Li et al., 2013; Scott et al., 1998).

Despite the effect of functional groups, the inherent caveats and discrepancy of the kinetic determination methods may also bring errors and/or uncertainty for evaluating the reactivity. Many studies used the indirect method with a RC, but this method assumes constant radiation/quantum yield in the presence of different RCs, and thus yields higher uncertainty than the direct method (Yu, 2004). In addition, if the k value of RC with $O_2^{\bullet-}$ is misestimated, the inaccuracy will unavoidably propagate to TC.

It is widely accepted that $O_2^{\bullet-}$ exhibits low reactivity in water due to its high degree of solvation by water molecules (Smith et al., 2004). However, comparative studies concerning thermodynamic properties of $O_2^{\bullet-}$ in different solvents are scarce. As an important thermodynamic parameter, redox potential (E°, V) can be used to approximately describe the reactivity of a specific ROS (Table 1). To explore the solvation effect on E°, we calculated the E° of $O_2^{\bullet-}$ in different solvents. The relationship between E° of $O_2^{\bullet-}$ and the polarity index of solvent is illustrated in Fig. 9. The experimentally measured E° of $O_2^{\bullet-}$ in N, N-dimethylformamide (DMF), DMSO and water are in good agreement with the calculated values, indicating the reliability of the theoretical approach. In addition, the E° increases as the polarity of solvents increases, indicating that $O_2^{\bullet-}$ has stronger reducibility in organic solvents than in water.

2.2. Reaction Mechanisms

Overall, four mechanisms can be envisaged for $O_2^{\bullet-}$-induced reactions: (1) single electron transfer (SET), (2) nucleophilic substitution (S_N1 and S_N2), (3) hydrogen atom abstraction (HAA), and (4) radical

adduct formation (RAF) (Jin et al., 1993; Sawyer and Valentine, 1981).

2.2.1. SET pathway

The SET pathway appears to dominate the reactions of $O_2^{\bullet-}$ with organic compounds, and in the presence of metal ions, it could also trigger the well-known Haber-Weiss reaction (Sawyer et al., 1982; Wilshire and Sawyer, 1979). As a reductant, $O_2^{\bullet-}$ undergoes one-electron oxidation:

$$O_2^{\bullet-} + R \rightarrow R^{\bullet-} + O_2 \quad (32)$$

The SET mechanism can be confirmed by product radical anion. A previous study reported that the major product of $O_2^{\bullet-}$ with 3,5–di–*tert*–butylquinone (DTBQ) is the semiquinone radical anion (Sawyer et al., 2018). This radical anion confirms the SET mechanism. As an oxidant, $O_2^{\bullet-}$ reacts with various flavonoids (FVH–O^-) *via* transfer of an electron to $O_2^{\bullet-}$ (Pietta, 2000). The H_2O_2 yield was measured by the kinetic conductivity method, and it was equivalent to the total consumption of $O_2^{\bullet-}$. The reaction mechanism for FVH—O^- reducing $O_2^{\bullet-}$ to O_2^{2-} was proposed as follows:

$$O_2^{\bullet-} + FVH - O^- \rightarrow FVH - O^{\bullet} + O_2^{2-} \quad (33)$$

But O_2^{2-} is unstable and reacts quickly with water to give H_2O_2:

$$O_2^{2-} + 2H_2O \rightarrow H_2O_2 + 2OH^- \quad (34)$$

Theoretical calculation also provides a powerful tool to probe the SET reaction mechanism. Density functional theory (DFT) approach combined with Marcus theory was used to study the SET reaction between $O_2^{\bullet-}$ and carotenoids in different solvents (Galano et al., 2010). Two possible directions (*i.e.,* electron from $O_2^{\bullet-}$ as reductant to carotenoids, and from carotenoids to $O_2^{\bullet-}$ as oxidant) have been taken into account. The calculation results showed that electron transfer from $O_2^{\bullet-}$ to carotenoids was more energetically and kinetically favored regardless of solvents.

Although kinetics and thermodynamics are not connected *a priori*, there is empirical relationship (*i.e.*, Marcus theory) between rates of SET reaction and Gibbs free energy ($\Delta_r G^o_{SET}$) (Mayer, 2011). The activation barrier ($\Delta^{\ddagger}G^{\circ}$) and the nuclear reorganization energy (λ) can be described as:

$$\Delta^{\ddagger}G^{o} = \frac{(\lambda + \Delta_r G^o_{SET})^2}{4\lambda} \quad (35)$$

$$\lambda = \Delta_r E^o_{SET} - \Delta_r G^o_{SET} \quad (36)$$

where $\Delta_r E^o_{SET}$ is the energy difference between reactants and vertical products involving a change of charge and spin multiplicity with the same geometries. Then, the *k* value of SET can be calculated as follows (McNeill and Canonica, 2016):

$$k = \frac{k_d}{1 + \frac{k_d}{K_d Z}\left\{\exp\left[\left(\sqrt{\left(\frac{\Delta_r G^o_{SET}}{2}\right)^2 + \left(\frac{\lambda}{4}\right)^2} + \frac{\Delta_r G^o_{SET}}{2}\right) \Big/ RT\right] + \exp\left(\frac{\Delta_r G^o_{SET}}{RT}\right)\right\}} \quad (37)$$

where k_d is the diffusion-controlled *k* value for the formation of the precursor complex, K_d is the corresponding equilibrium constant, *Z* is the universal collision frequency factor (*i.e.,* 6×10^{11} s^{-1} in aqueous solution). To evaluate the antioxidant capacity of $O_2^{\bullet-}$, the SET reaction of $O_2^{\bullet-}$ with phenothiazine radical was calculated. With Marcus theory, the *k* value was calculated to be 7.84×10^9 M^{-1} s^{-1}, and the high *k* value indicates the excellent antioxidant capacity of $O_2^{\bullet-}$ (Iuga et al., 2015).

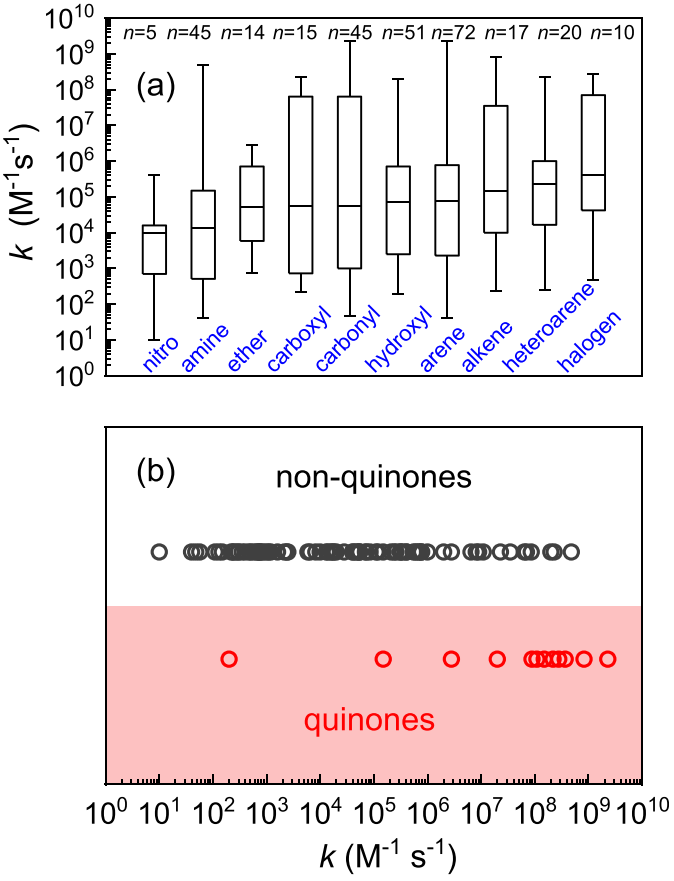

Fig. 8. (a) Box plot of *k* ($M^{-1}s^{-1}$) for the reactions of $O_2^{\bullet-}$ and different target compounds. These compounds are classified into subgroups based on their functional groups. (The bottom and top of each box represent the lower and upper quartiles, respectively. While the bottom and top bars represent the minimum and maximum values, respectively. Horizontal line denotes the median, and *n* refers to the number of data for each subgroup) (b) Comparison of the *k* values (M^{-1} s^{-1}) for the reactions of $O_2^{\bullet-}$ with quinones (red shadowed) and non−quinones (grey shadowed) compounds.

2.2.2. Nucleophilic pathway

Nucleophilicity is considered to be the most unique characteristic of $O_2^{\bullet-}$ especially in aprotic solvents (McDonald and Chowdhury, 1985; Merritt and Sawyer, 1970), but $O_2^{\bullet-}$ does not display this feature in water due to its strong solvation and rapid disproportionation (Bryantsev et al., 2011; Johnson and Nidy, 1975). A representative nucleophilic reaction occurs between $O_2^{\bullet-}$ and alkyl halides, which consists in a first-order reaction *via* bimolecular nucleophilic substitution (S_N2), that is, the bond–forming and bond–breaking of the reaction occur simultaneously. A general S_N2 mechanism of $O_2^{\bullet-}$ with alkyl halides is here proposed (R refers to alkyl group, X to the halogen atom) (Gibian and Ungermann, 1976):

$$RX + O_2^{\bullet-} \rightarrow RO_2^{\bullet} + X^- \quad (38)$$

An electron is initially transferred, followed by the collapse of a

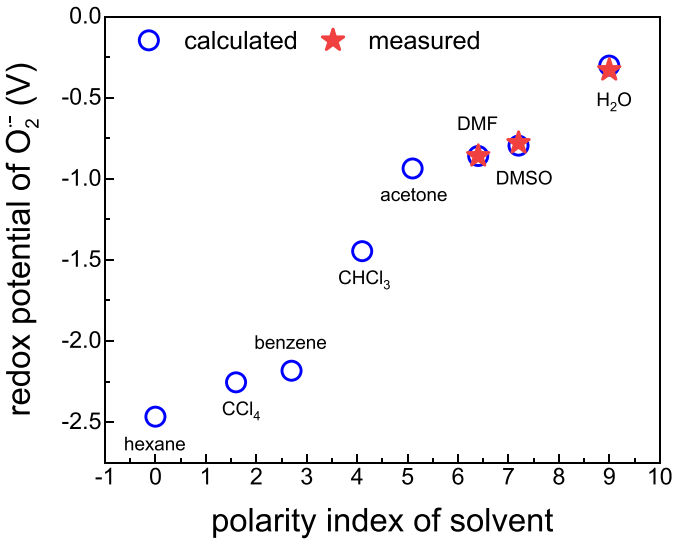

Fig. 9. The redox potential of $O_2^{\bullet-}$ (circles) as a function of polarity index (unitless) of solvents from the least polar (hexane) to the most polar (water). The energy calculations were performed at the M06−2X/6−311++G** level with SMD solvation models. The measured values (stars) were from literature.

radical pair.

$$RX + O_2^{\bullet-} \rightarrow [O_2^{\bullet-} \cdots R^+ \cdots X^-] \rightarrow RO_2^{\bullet} + X^- \quad (39)$$

Maeda et al. (2005) studied the reaction kinetics between $O_2^{\bullet-}$ and bis (2,4-dinitrobenzenesulfonyl) fluoresceins (DF) with CV in an XO/HPX system. They proposed that DF is transformed by $O_2^{\bullet-}$ *via* nucleophilic pathway, rather than SET since DF requires at least two $O_2^{\bullet-}$ to form one molecule of fluorescein that loses the benzenesulfonyl group. In addition, they reported that four halogenated derivatives of DF exhibited irreversible cathodic potentials at –0.60, –0.63, –0.63, and –0.65 V *vs.* Ag/AgCl, respectively. This result excluded the possible reduction mechanisms due to the small difference in reduction potentials. Note, the increased substitution by the methyl group would increase the steric repulsion with the incoming nucleophile $O_2^{\bullet-}$, slowing the reaction rate (Roberts Jr et al., 1983). For alkyl esters, DFT calculations supported that the addition of one and two methyl groups increases the activation free energy by 1.7 and 3.6 kcal mol^{-1}, respectively (Bryantsev et al., 2011). This could be explained by the increasing steric hindrance with the increase of alkyl groups.

2.2.3. *HAA pathway*

The HAA mechanism can be described by:

$$RH + O_2^{\bullet-} \rightarrow R^{\bullet} + HO_2^- \quad (40)$$

However, the HAA pathway has not been frequently reported, since $O_2^{\bullet-}$ is a weak oxidant and the low oxidation potential makes it difficult to abstract H atoms from most C–H, N–H, and O–H groups (Sawyer et al., 1978). For example, the reactivity of $O_2^{\bullet-}$ with hydrophenazines, flavins, and hydroxylamine suggested the occurrence of a HAA mechanism, as these compounds easily transfer hydrogen atoms, and $O_2^{\bullet-}$ adducts *via* RAF or O_2 formation *via* SET were not detected in the system (Nanni Jr and Sawyer, 1980). Meanwhile, the reaction mechanism of thymoquinone with $O_2^{\bullet-}$ in different phases (*e.g.,* gas, water, and benzene) was explored using computational chemistry. The theoretical result demonstrated a HAA process with a low activation energy barrier of ~2.5 kcal mol^{-1} (Galano et al., 2010). The calculated thermodynamic properties including bond dissociation enthalpy, ionization potential, and proton dissociation enthalpy, indicated that the hydrogen atoms at the isopropyl and methyl groups are readily abstracted.

The concerted double hydrogen transfer may be a specific mode of HAA, where a proton (H^+) and a hydrogen atom transfer from target compounds to $O_2^{\bullet-}$ simultaneously (Prasad and Mishra, 2015):

$$R - H_n + O_2^{\bullet-} \rightarrow R - H_{n-2}^{\bullet-} + H_2O_2 \quad (41)$$

R–H_n is the compound with n hydrogen atoms, and $R - H_{n-2}^{\bullet-}$ is the compound/radical with 2 hydrogen atoms abstracted. A previous CV study of the reaction of $O_2^{\bullet-}$ with ascorbic acid provided electrochemical and spectrophotometric evidence that the primary step of this reaction appears to be a concerted transfer of a proton and hydrogen atom from ascorbic acid to $O_2^{\bullet-}$, producing dehydroascorbate anion radical and H_2O_2 (Sawyer et al., 1985). Interestingly, the mechanism of $O_2^{\bullet-}$ with sulforaphane was investigated by means of DFT (Prasad and Mishra, 2015), and the results demonstrated that it is a concerted double hydrogen transfer mechanism; indeed, the calculated $\Delta_r G^\circ$ was in the range of −29.9 to −20.1 kcal mol^{-1} with almost barrierless activation energy (−5.1 to −1.7 kcal mol^{-1}).

The kinetic isotope effects (KIE) technique has also been used to diagnose HAA reaction mechanisms (Westheimer, 1961). The KIE can be measured as the rate ratio (k_H/k_D) of two isotopes in separate experiments, where H atoms in one reactant are replaced with deuterium:

$$KIE = \frac{k_H}{k_D} = \frac{\exp\left[-\Delta G_H^{\ddagger}/RT\right]}{\exp\left[-\Delta G_D^{\ddagger}/RT\right]} = \exp\left[-\frac{\Delta G_H^{\ddagger} - \Delta G_D^{\ddagger}}{RT}\right] \quad (42)$$

where k_H is the rate for normal reactants and k_D is the rate for deuterated reactants. Moreover, $\Delta G_H^{\ddagger}$ and $\Delta G_D^{\ddagger}$ are the corresponding activation energy barriers of normal reactants and deuterated reactants, respectively. One can confirm the HAA reaction mechanism with a KIE value greater than 2, while a KIE value in the range of 0.7~1.5 indicates otherwise. The KIE technique was used to elucidate the reaction mechanism between $O_2^{\bullet-}$ and diphenylhydrazine (Sacramento and Goldberg, 2019). The substitution of deuterium for the N–H hydrogens of diphenylhydrazine resulted in a significant decrease of the k value (k_H/k_D = 9.2). The large KIE value provides compelling evidence for the HAA mechanism. Note, the KIE technique can be utilized not only for $O_2^{\bullet-}$ but also for mechanistic diagnosis in other radical systems, as well as in non-radical systems. For example, the reaction mechanism of chlorine radical ($Cl^{\bullet}$) with methane was reckoned to be HAA by the KIE technique with a k_H/k_D value higher than 6 (Li et al., 2014).

2.2.4. *RAF pathway*

The RAF pathway involves target compounds with unsaturated bond (s), and it is not a common reaction mode for $O_2^{\bullet-}$ (Stemmler et al., 1994). Although there is similarity between RAF and S_N2, no functional group elimination occurs in the RAF mechanism. The formation of adducts with $O_2^{\bullet-}$ has been documented for alcohols, ketones, phenols, tetrachlorodioxins, polyethers, phthalates, and trichothecenes (Hassan et al., 2016):

$$R + O_2^{\bullet-} \rightarrow ROO^{\bullet-} \quad (43)$$

The addition of $O_2^{\bullet-}$ to a diamagnetic cyclic nitrone is the most common RAF pathway, and its spin adduct product exhibits a characteristic EPR spectrum. Many spin traps (*e.g.,* BMPO and DMPO) can react covalently with $O_2^{\bullet-}$, forming more stable adducts with longer half–lives (Abbas et al., 2014). These stable adducts can be used to quantify the concentration of $O_2^{\bullet-}$. However, $O_2^{\bullet-}$ under RAF pathway is usually characterized by low k value (below 10^6 M^{-1} s^{-1}) (Durand et al., 2008; Nagy et al., 2009). The k values of $O_2^{\bullet-}$ with pyrogallol and n-propyl gallate were measured to be 3.4×10^5 and 2.6×10^5 M^{-1} s^{-1}, respectively, by pulse radiolysis (Deeble et al., 1988). The reaction pathway was determined to be RAF, and is initiated by $O_2^{\bullet-}$ addition to the site where the second phenolic hydroxyl is located. After two additions of $O_2^{\bullet-}$ and eliminations of HO_2^-, a new product exhibiting no absorption at 300 to 600 nm was formed.

3. Environmental implications

3.1. Maintenance of biogeochemical iron cycle

The relatively low redox potential of $O_2^{\bullet-}$ facilitates its role in mediating the redox reactions of various metals and maintaining their biogeochemical cycles (Learman et al., 2011; Wang et al., 2018b). For example, as a micronutrient in both aquatic and terrestrial ecosystems, iron participates in numerous biogeochemical processes, including the coupling of microbial ammonium and methane oxidation with Fe(III) reduction. Iron is mainly occurring in ferric (Fe^{3+}) and ferrous form (Fe^{2+}) (Kappler et al., 2021). Despite its higher thermodynamic stability, Fe^{3+} undergoes rapid hydrolysis and precipitation at circumneutral pH, hindering its biological uptake. In contrast, the reduced form Fe^{2+} is much more soluble and thus possesses higher bioavailability. However, in surface waters, Fe^{2+} is rapidly oxidized to Fe^{3+} at circumneutral pH, which in turn restricts iron bioavailability (Kirby et al., 2020). $O_2^{\bullet-}$ can reduce Fe^{3+} to Fe^{2+}, thus increasing the bioavailability of iron. Rose and Waite (2006) conducted a series of experiments using FeLume chemiluminescence for detection of total ferrous iron and $O_2^{\bullet-}$ in natural waters. They found that an addition of SOD, a specific enzyme that catalyzes the disproportionation of $O_2^{\bullet-}$, resulted in a slow decrease in the rate of Fe^{2+} formation, indicating that $O_2^{\bullet-}$ is involved in the formation of Fe^{2+}. Further, they determined the reaction rate constant between $O_2^{\bullet-}$ and Fe^{3+} to be $1.5 \times 10^5\ M^{-1}s^{-1}$. This value confirms that $O_2^{\bullet-}$ is primarily responsible for transient levels of Fe^{2+} in natural waters. Thus, $O_2^{\bullet-}$ is of great importance in sunlit open−ocean waters to maintain the geochemical cycle of Fe^{2+}/Fe^{3+}.

3.2. Mediation of nanoparticle formation

The antibacterial properties of silver have long been acknowledged (Davies and Etris, 1997). A plethora of studies illustrate that silver nanosized particles (AgNPs) exhibit a remarkable cytotoxicity toward various bacteria such as *Staphylococcus aureus, Vibrio cholerae,* and *Escherichia coli* (Morones et al., 2005). Although many approaches (*e.g.,* Brust–Schiffrin and Turkevich methods) can be used to synthesize AgNPs, these methods were used in non–polar medium (*e.g.,* toluene) and with interfacial carriers (*i.e.,* tetra–*n*–alkylammonium) which are not applicable to many aqueous antibacterial scenarios (Lee and Jun, 2019). As a result, the use of $O_2^{\bullet-}$ for AgNP synthesis has been proposed:

$$O_2^{\bullet-} + Ag^+ \rightarrow AgNP + O_2 \quad (44)$$

Ono et al. (1977) studied the formation process of $O_2^{\bullet-}$ by the decomposition of H_2O_2 in the presence of $Ag/AlCl_3$ in aqueous solutions, and they found that the concentration of $O_2^{\bullet-}$ increases with the reaction between H_2O_2 and $Ag/AlCl_3$. The $O_2^{\bullet-}$ concentration was measured to be as high as 0.62 mM, indicating the high catalytic performance of the $Ag/AlCl_3$ material. They also observed that $O_2^{\bullet-}$ reduces Ag^+ to AgNPs, exerting strong bactericidal activity towards *Salmonella typhi* and *Escherichia coli*. However, they did not quantify the formation rate of AgNPs. Jones et al. (2011) built their study upon Ono *et al.*, and they investigated this reaction by directly measuring the decay of $O_2^{\bullet-}$ at different concentrations of Ag^+. Fig. 10a and b show the formation rate of AgNPs under various concentrations of Ag^+ or $O_2^{\bullet-}$, and the schematic diagram is shown in Fig. 10c. The k value was measured to be $64.5 \pm 16.3\ M^{-1}s^{-1}$ in the initial stage of the reaction (Eq. 44), indicating extremely slow kinetics. However, with the formation of heterogeneous AgNPs, this reaction becomes faster with k value of $6 \times 10^5\ M^{-1}s^{-1}$, approximately 4 orders of magnitude higher than that in the initial stage. As AgNPs are produced, they rapidly react with $O_2^{\bullet-}$ forming electron charged AgNPs (Ag^{0-}). This newly formed species subsequently accelerates the transfer of electrons from $O_2^{\bullet-}$ to Ag^+, resulting in formation of more AgNPs. This study opens new possibilities to generate AgNPs for antibacterial purposes in aqueous solution.

3.3. Desorption of contaminants

In situ chemical oxidation (ISCO) is gaining an increasing popularity for the remediation of organic contaminants in soils and groundwater (Furman et al., 2009). Within this treatment scenario, the efficiency depends on the desorption rate of contaminants from soils and aquifer solids/organic matter. Compared to the conventional gas-purging technology, many studies reported that $O_2^{\bullet-}$−based processes (*e.g.*, modified Fenton's reaction) can simultaneously desorb and degrade contaminants. Watts et al. (1999) studied the mechanism for desorption of chloroaliphatic compounds from a silty loam soil, and they found that $O_2^{\bullet-}$ is responsible for enhanced desorption and reduction of hydrophobic compounds in vigorous Fenton-like conditions. This technique fits into the framework of the sustainable development, showing promise as a prospective ISCO process.

Although the enhanced treatment of adsorbed contaminants has been documented in modified Fenton's reactions, the species responsible for the enhanced desorption have not been clarified yet. Previous studies suggested that two reactive species ($O_2^{\bullet-}$ and HO_2^-, that is, deprotonated H_2O_2) may be involved. In order to distinguish their contribution, KO_2 was used as $O_2^{\bullet-}$ source in a dodecane−silica system (Corbin et al., 2007). The addition of 1 M KO_2 to the system resulted in 22% dodecane desorption from silica, while 3 M KO_2 produced 82% desorption. For comparison, the processes were investigated in the presence of HO_2^-, but no significant desorption was observed over 3 hr. This could be explained in that $O_2^{\bullet-}$ might partition into the dodecane layer at the mineral silica surface *via* hydrogen bonding, and displace dodecane from surface adsorption sites, thus promoting desorption (Fig. 11).

In addition to desorption, $O_2^{\bullet-}$ also plays a part in the degradation of contaminants at the surface of materials. In a TiO_2–catalyzed system, the $O_2^{\bullet-}$ at the surface of TiO_2 degraded microcystin–LR (MC–LR) at a k value of $10^7\ M^{-1}\ s^{-1}$ (Feitz and Waite, 2003). There are two degradation modes for MC–LR: *i*) the generated $O_2^{\bullet-}$ induces a direct degradation of adsorbed MC–LR on TiO_2 surface; *ii*) the generated $O_2^{\bullet-}$ on the surface is released and reacts with MC–LR in the bulk solution. The results also illustrated that almost 40% MC–LR was desorbed from the TiO_2 surface within 10 min, and both the adsorbed and desorbed MC–LR could be degraded completely within 20 min. It is noteworthy that at high concentration of DO, the generated MC–LR$^{\bullet-}$ can rapidly form a peroxyl radical that may terminate $O_2^{\bullet-}$ in turn. It should also be noted, that irradiated TiO_2 yields a very wide range of reactive species (bulk and surface-adsorbed $^{\bullet}OH$, surface-trapped holes, surface-trapped electrons) that in the general case make it very difficult to identify a single species that may be involved in the degradation of a substrate.

3.4. Synergisms for degradation of contaminants

Superoxide radical has the potential to synergistically interact with other ROS, thereby facilitating the degradation of contaminants in homogenous and heterogeneous systems. Many studies reported that $O_2^{\bullet-}$ mediates the degradation of contaminants in photocatalytic systems (Fig. 12). Xu et al. (2021) studied the photocatalytic decomposition of sodium pentachlorophenate (NaPCP) by a model photocatalyst consisting in oxygen-deficient $Bi@Bi_2MoO_6$ (Bi-BMO-OVs). The formation of $O_2^{\bullet-}$ was initiated by the reaction of DO with photoinduced electrons. In the batch experiments, it was found that the addition of SOD inhibited 39.3% of NaPCP degradation after 2 hr treatment. Meanwhile, the addition of other scavengers (IPA, triethanolamine, and β-carotene for $^{\bullet}OH$, h^+ and $^1O_2$, respectively) also showed significant inhibition of NaPCP degradation, indicating the synergism between $O_2^{\bullet-}$ and these reactive species.

Many studies also focused on the degradation of contaminants with $O_2^{\bullet-}$ in aqueous solution. Guo et al. (2021a) measured a series of reaction rate constants of $O_2^{\bullet-}$ using the competition kinetics method in a

XAN/XOD system; they reported that the k value between perfluorooctanoic acid (PFOA) and $O_2^{\bullet-}$ was high, up to 6.4×10^7 M^{-1} s^{-1}, indicating a great abatement performance. Nevertheless, a recent study showed that $O_2^{\bullet-}$ exhibited weak reactivity towards PFCAs since the measured k values (in the order of 10^3 M^{-1} s^{-1}) were approximately 4 orders of magnitude lower than that of Guo *et al.* (Bai et al., 2022). It seems that the reported high k value may be suspect, as many other studies explicitly indicated that $O_2^{\bullet-}$ alone exhibits extremely low degradation efficiency towards PFCAs (Bai et al., 2022; Javed et al., 2020; Xia et al., 2022). Further, the synergistic effects of $O_2^{\bullet-}$ with other ROS such as $^{\bullet}OH$ were frequently reported in different systems. A previous study demonstrated that catalyzed hydrogen peroxide could effectively enhance the mineralization of sorbed benzo[a]pyrene (BaP) in soils. In a Fenton system, Fe^{2+} acts as a catalyst to generate a set of ROS including $^{\bullet}OH$, $O_2^{\bullet-}$, and $HO_2^{\bullet}$ (Watts et al., 2002). The Fe^{2+}-initiated process provided an ideal treatment matrix with high reactivity and selectivity, enabling BaP to be desorbed and degraded in a single step. Specifically, $O_2^{\bullet-}$ initiates the desorption process of hydrophobic BaP from the soil, while $^{\bullet}OH$ degrades the contaminants. This synergistic process is particularly advantageous because $^{\bullet}OH$ may be poorly effective in the oxidation of organic contaminants that are bound to heterogeneous phases such as soils (Chin et al., 1997; Wei-Haas et al., 2014).

4. Conclusion and outlook

Superoxide radical has been studied for over a century in fields ranging from biology to chemistry, and for much of that time emphasis was placed in understanding its biological and chemical functions. It was not until the end of the last century that scientists began to appreciate the broader role of $O_2^{\bullet-}$ in biogeochemical cycles, toxicology, and pollution remediation. Within this context, this review covered the generation and detection methods of $O_2^{\bullet-}$, and advantages and disadvantages of each method were critically compared. We summarized the k values of $O_2^{\bullet-}$ with contaminants covering a wide structural and reactivity diversity. The comparative results indicate that $O_2^{\bullet-}$ shows no evident selectivity towards contaminants with different functional groups, but the class of quinones demonstrates a higher reactivity than non-quinones. We also evaluated the reaction mechanisms of $O_2^{\bullet-}$ with different TCs, and finally we presented its environmental implications in different scenarios.

There are still several significant challenges remaining in this research field. In particular, previous studies developed QSAR models to predict the reactivity of $O_2^{\bullet-}$ towards various TCs, but a proper achievement of this goal requires high quality kinetic data. The inherent caveats and discrepancy of the kinetic determination methods unavoidably lead to inaccuracy of data, rendering QSAR models for this radical less convincing compared to other reactive species. In addition,

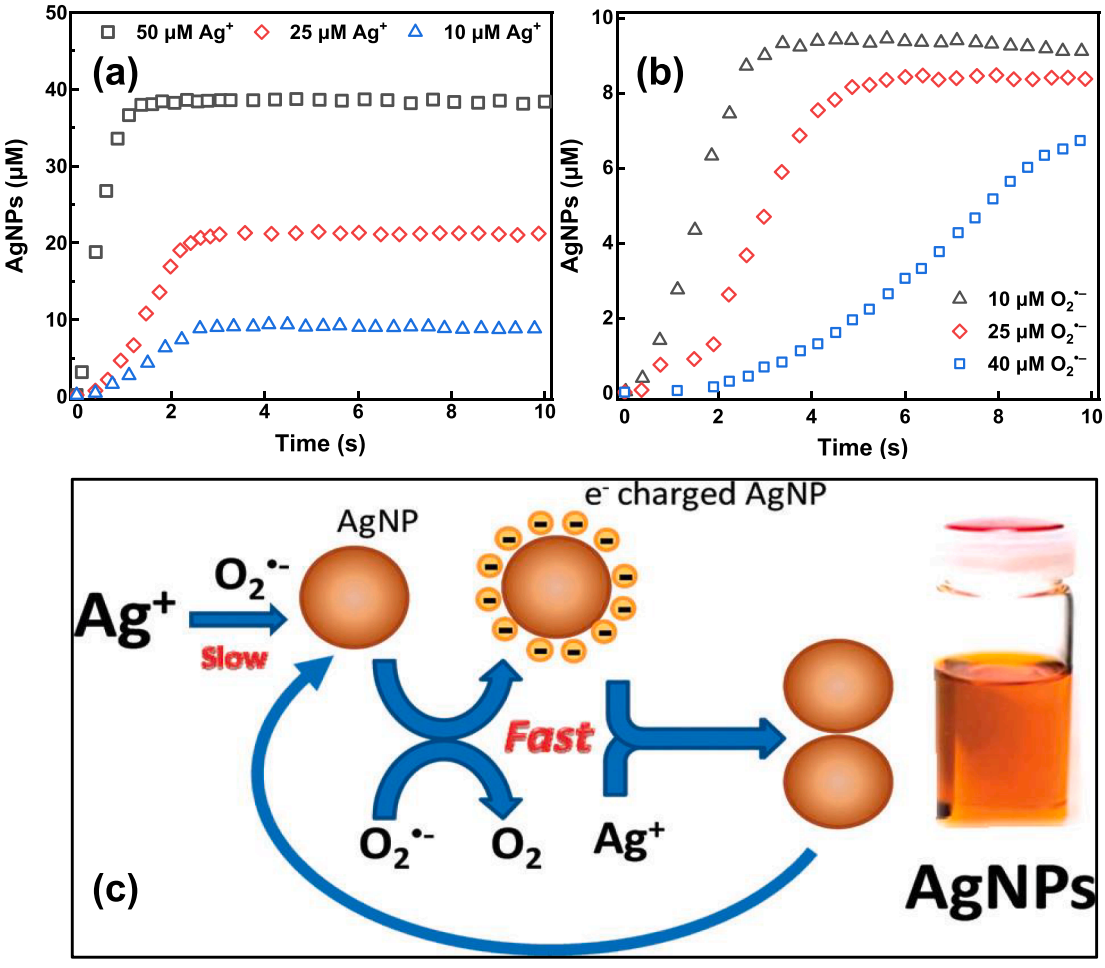

Fig. 10. Increase in AgNP concentration over time: (a) $[O_2^{\bullet-}]_0 = 40$ μM with different $[Ag^+]_0$; (b) $[Ag^+]_0 = 10$ μM with different $[O_2^{\bullet-}]_0$. Experiments were performed in a pH 9.5, 2 mM total carbonate solution containing 0.5 μM DTPA. (c) Schematic illustrating the $O_2^{\bullet-}$-mediated reduction of silver(I) ions (Ag^+) resulting in the production of silver nanoparticles (AgNPs). The initial reduction of Ag^+ by $O_2^{\bullet-}$ is slow. As AgNPs are produced, the reaction accelerates as AgNPs react rapidly with $O_2^{\bullet-}$ to produce electron-charged AgNPs that subsequently and rapidly transfer electrons to Ag^+, resulting in production of more AgNPs. (This Fig. is reproduced from Figs. 4 and 5 in reference Jones et al. (2011), Copyright 2011 American Chemical Society.)

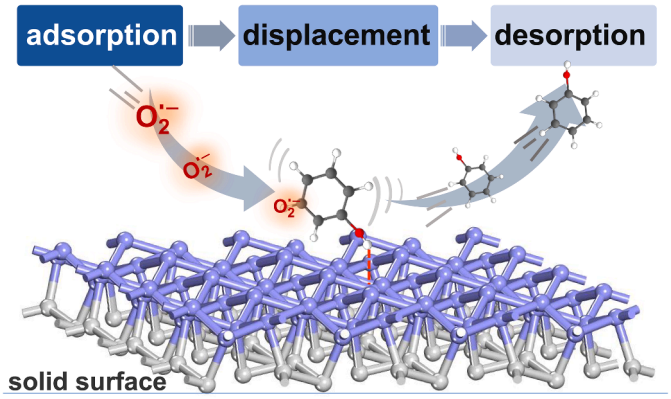

Fig. 11. Adsorption, displacement, and desorption behavior of contaminants by $O_2^{\bullet-}$ on the solid surface of materials.

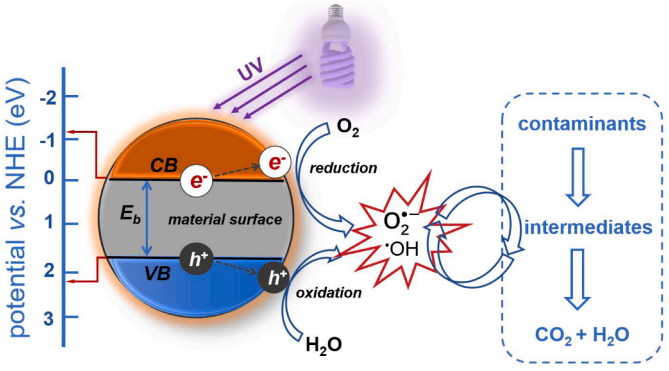

Fig. 12. Heterogeneous photocatalysis involving $O_2^{\bullet-}$ for contaminant degradation: photoexcitation of an electron from the semiconductor valence band to the conduction band, forming $O_2^{\bullet-}$ in the presence of DO, and leaving a positive hole in the valence band to form •OH. (The red arrows point to the redox potentials of electron and hole, respectively).

experimental and theoretical results suggest that $O_2^{\bullet-}$ is often not responsible for the direct degradation of contaminants, which is confirmed by the *k* values data collected in Table 4. The observed $O_2^{\bullet-}$-mediated degradation in heterogeneous systems cannot be simply attributed to its reactivity, but rather to synergistic effect with other ROS. Further, despite the desorption ability of $O_2^{\bullet-}$ reported in many heterogeneous systems, a systematic knowledge of desorption mechanisms is still missing. Delving into the intricacies of these mechanisms is imperative to exploit $O_2^{\bullet-}$ for the remediation of contaminated groundwater and subsurface soils. It is also noteworthy that, the current research on the generation mechanism of $O_2^{\bullet-}$ by marine microalgae and their intricate interplays is still in its infancy. Efforts need to be directed to answering questions on the large scale, such as quantitation of the contribution of $O_2^{\bullet-}$ from microalgae to the overall $O_2^{\bullet-}$ production in natural aquatic systems and more precise understanding of the environmental significance of $O_2^{\bullet-}$ in biogeochemical processes.

CRediT authorship contribution statement

Zonghao Luo: Writing – original draft, Investigation, Data curation, Conceptualization. **Yiqi Yan:** Writing – review & editing, Investigation. **Richard Spinney:** Writing – review & editing, Validation. **Dionysios D. Dionysiou:** Writing – review & editing, Validation. **Frederick A. Villamena:** Writing – review & editing, Resources. **Ruiyang Xiao:** Writing – review & editing, Supervision, Resources, Funding acquisition. **Davide Vione:** Writing – review & editing, Supervision, Funding acquisition.

Declaration of competing interest

The authors declare that they have no known competing financial interests or personal relationships that could have appeared to influence the work reported in this paper.

Data availability

Data will be made available on request.

Acknowledgments

Funding from National Natural Science Foundation of China (No. 22376220 and No. 52121004) is gratefully acknowledged. DV also acknowledges support from Project CH4.0 under the MUR program "Dipartimenti di Eccellenza 2023-2027" (CUP: D13C22003520001) and Next Generation EU – PNRR project GRINS (Growing Resilient, INclusive, and Sustainable), PE9 - spoke 6 (PE00000018, CUP D13C22002160001).

Supplementary materials

Supplementary material associated with this article can be found, in the online version, at doi:10.1016/j.watres.2024.122023.

References

Abbas, K., Hardy, M., Poulhès, F., Karoui, H., Tordo, P., Ouari, O., Peyrot, F., 2014. Detection of superoxide production in stimulated and unstimulated living cells using new cyclic nitrone spin traps. Free. Radical Bio. Med. 71, 281–290.
Bai, L., Jiang, Y., Xia, D., Wei, Z., Spinney, R., Dionysiou, D.D., Minakata, D., Xiao, R., Xie, H.-B., Chai, L., 2022. Mechanistic understanding of superoxide radical-mediated degradation of perfluorocarboxylic acids. Environ. Sci. Technol. 56 (1), 624–633.
Beauchamp, C., Fridovich, I., 1971. Superoxide dismutase: improved assays and an assay applicable to acrylamide gels. Anal. Biochem. 44 (1), 276–287.
Bednarczyk, D., Ekins, S., Wikel, J.H., Wright, S.H., 2003. Influence of molecular structure on substrate binding to the human organic cation transporter, hOCT1. Mol. Pharmacol. 63 (3), 489–498.
Berger, C., Datta, H., Horrocks, B., 2011. Simulation of generation–collection experiments with homogeneous kinetics: application to electrochemical investigation of superoxide radical anion generation by osteoclasts on bone. Phys. Chem. Chem. Phys. 13 (12), 5288–5297.
Bielski, B.H., 1978. Reevaluation of the spectral and kinetic properties of HO_2 and O_2^- free radicals. Photochem. Photobiol. 28 (4-5), 645–649.
Bielski, B.H., Allen, A.O., 1977. Mechanism of the disproportionation of superoxide radicals. J. Phys. Chem. 81 (11), 1048–1050.
Bielski, B.H., Arudi, R.L., 1983. Preparation and stabilization of aqueous/ethanolic superoxide solutions. Anal. Biochem. 133 (1), 170–178.
Bielski, B.H., Cabelli, D.E., Arudi, R.L., Ross, A.B., 1985. Reactivity of HO_2/O_2^- radicals in aqueous solution. J. Phys. Chem. Ref. Data 14 (4), 1041–1100.
Bielski, B.H.J., Cabelli, D.E., 1991. Highlights of current research involving superoxide and perhydroxyl radicals in aqueous solutions. Int. J. Radiat. Biol. 59 (2), 291–319.
Bors, W., Michel, C., Saran, M., Lengfelder, E., 1978. Kinetic investigations of the autoxidation of adrenalin. Z. Naturforsch. C 33 (11-12), 891–896.
Brigelius, R., Spöttl, R., Bors, W., Lengfelder, E., Saran, M., Weser, U., 1974. Superoxide dismutase activity of low molecular weight Cu^{2+}-chelates studied by pulse radiolysis. FEBS Lett. 47 (1), 72–75.
Bryantsev, V.S., Giordani, V., Walker, W., Blanco, M., Zecevic, S., Sasaki, K., Uddin, J., Addison, D., Chase, G.V., 2011. Predicting solvent stability in aprotic electrolyte Li–air batteries: nucleophilic substitution by the superoxide anion radical ($O_2^{\bullet-}$). J. Phys. Chem. A 115 (44), 12399–12409.
Burns, J.M., Cooper, W.J., Ferry, J.L., King, D.W., DiMento, B.P., McNeill, K., Miller, C.J., Miller, W.L., Peake, B.M., Rusak, S.A., 2012. Methods for reactive oxygen species (ROS) detection in aqueous environments. Aquat. Sci. 74, 683–734.
Butler, J., Hoey, B.M., 1986. The apparent inhibition of superoxide dismutase activity by quinones. Free Radical Bio. Med. 2 (1), 77–81.
Buxton, G.V., Greenstock, C.L., Helman, W.P., Ross, A.B., 1988. Critical review of rate constants for reactions of hydrated electrons, hydrogen atoms and hydroxyl radicals (•OH/•O⁻ in aqueous solution. J. Phys. Chem. Ref. Data 17 (2), 513–886.
Chern, C.-I., DiCosimo, R., De Jesus, R., San Filippo Jr, J., 1978. A study of superoxide reactivity. Reaction of potassium superoxide with alkyl halides and tosylates. J. Am. Chem. Soc. 100 (23), 7317–7327.
Chin, D.H., Chiericato Jr, G., Nanni Jr, E.J., Sawyer, D.T, 1982. Proton-induced disproportionation of superoxide ion in aprotic media. J. Am. Chem. Soc. 104 (5), 1296–1299.

Chin, Y.-P., Aiken, G.R., Danielsen, K.M., 1997. Binding of pyrene to aquatic and commercial humic substances: the role of molecular weight and aromaticity. Environ. Sci. Technol. 31 (6), 1630–1635.
Corbin, J.F., Teel, A.L., Allen-King, R.M., Watts, R.J., 2007. Reactive oxygen species responsible for the enhanced desorption of dodecane in modified Fenton's systems. Water Environ. Res. 79 (1), 37–42.
Davies, R.L., Etris, S.F., 1997. The development and functions of silver in water purification and disease control. Catal. Today 36 (1), 107–114.
Deeble, D.J., Parsons, B.J., Phillips, G.O., Schuchmann, H.-P., Von Sonntag, C, 1988. Superoxide radical reactions in aqueous solutions of pyrogallol and N-propyl gallate: The involvement of phenoxyl radicals. A pulse radiolysis study. Int. J. Radiat. Biol. 54 (2), 179–193.
Dietzel, P.D.C., Kremer, R.K., Jansen, M., 2004. Tetraorganylammonium superoxide compounds: Close to unperturbed superoxide ions in the solid state. J. Am. Chem. Soc. 126 (14), 4689–4696.
Divišek, J., Kastening, B., 1975. Electrochemical generation and reactivity of the superoxide ion in aqueous solutions. J. Electroanal. Chem 65 (2), 603–621.
Dohrmann, J.K., Bergmann, B., 1995. Equilibria and rates of redox reactions involving the 2-tert-butyl-1,4-benzosemiquinone radical in aqueous solution: an investigation by potentiometry, ESR, and pulse radiolysis. J. Phys. Chem. 99 (4), 1218–1227.
Durand, G., Choteau, F., Pucci, B., Villamena, F.A., 2008. Reactivity of superoxide radical anion and hydroperoxyl radical with α-phenyl-n-tert-butylnitrone (PBN) derivatives. J. Phys. Chem. A 112 (48), 12498–12509.
Durot, S., Lambert, F., Renault, J.P., Policar, C., 2005. A pulse radiolysis study of catalytic superoxide radical dismutation by a Manganese (ii) complex with an N-tripodal ligand. Wiley Online Library.
Ervin, K.M., Anusiewicz, I., Skurski, P., Simons, J., Lineberger, W.C., 2003. The only stable state of O_2^- is the X 2Πg ground state and it (still!) has an adiabatic electron detachment energy of 0.45 eV. J. Phys. Chem. A 107 (41), 8521–8529.
Feitz, A.J., Waite, T.D., 2003. Kinetic modeling of TiO_2-catalyzed photodegradation of trace levels of microcystin-LR. Environ. Sci. Technol. 37 (3), 561–568.
Felix, K., Lengfelder, E., Hartmann, H.-J., Weser, U., 1993. A pulse radiolytic study on the reaction of hydroxyl and superoxide radicals with yeast Cu (I)-thionein. BBA Protein Struct. Mol. Enzymol. 1203 (1), 104–108.
Fenton, H.J.H., 1894. LXXIII.—Oxidation of tartaric acid in presence of iron. J. Chem. Soc. Trans. 65, 899–910.
Fielden, E.M., Roberts, P.B., Bray, R.C., Lowe, D.J., Mautner, G.N., Rotilio, G., Calabrese, L., 1974. The mechanism of action of superoxide dismutase from pulse radiolysis and electron paramagnetic resonance. Evidence that only half the active sites function in catalysis. Biochem. J. 139 (1), 49–60.
Fujii, M., Ito, H., Rose, A.L., Waite, T.D., Omura, T., 2008. Superoxide-mediated Fe(II) formation from organically complexed Fe(III) in coastal waters. Geochim. Cosmochim. Ac. 72 (24), 6079–6089.
Fujii, M., Otani, E., 2017. Photochemical generation and decay kinetics of superoxide and hydrogen peroxide in the presence of standard humic and fulvic acids. Water. Res. 123, 642–654.
Fujita, M., Tsuruta, R., Kasaoka, S., Fujimoto, K., Tanaka, R., Oda, Y., Nanba, M., Igarashi, M., Yuasa, M., Yoshikawa, T., 2009. In vivo real-time measurement of superoxide anion radical with a novel electrochemical sensor. Free. Radical Bio. Med. 47 (7), 1039–1048.
Furman, O., Laine, D.F., Blumenfeld, A., Teel, A.L., Shimizu, K., Cheng, I.F., Watts, R.J., 2009. Enhanced reactivity of superoxide in water−solid matrices. Environ. Sci. Technol. 43 (5), 1528–1533.
Galano, A., Vargas, R., Martínez, A., 2010. Carotenoids can act as antioxidants by oxidizing the superoxide radical anion. Phys. Chem. Chem. Phys. 12 (1), 193–200.
Garg, S., Rose, A.L., Waite, T.D., 2011. Photochemical production of superoxide and hydrogen peroxide from natural organic matter. Geochim. Cosmochim. Ac. 75 (15), 4310–4320.
Georgiou, C.D., Sun, H.J., McKay, C.P., Grintzalis, K., Papapostolou, I., Zisimopoulos, D., Panagiotidis, K., Zhang, G., Koutsopoulou, E., Christidis, G.E., 2015. Evidence for photochemical production of reactive oxygen species in desert soils. Nat. Commun. 6 (1), 7100.
Gibian, M.J., Ungermann, T., 1976. Reaction of tert-butyl hydroperoxide anion with dimethyl sulfoxide. On the pathway of the superoxide-alkyl halide reaction. J. Org. Chem. 41 (14), 2500–2502.
Goldstein, S., Czapski, G., 1990. A reinvestigation of the reaction of desferrioxamine with superoxide radicals. A pulse radiolysis study. Free Radical Res 11 (4-5), 231–240.
Goldstein, S., Czapski, G., Meyerstein, D., 1990. A mechanistic study of the copper (II)-peptide-catalyzed superoxide dismutation. A pulse radiolysis study. J. Am. Chem. Soc. 112 (18), 6489–6492.
Goldstone, J.V., Voelker, B.M., 2000. Chemistry of superoxide radical in seawater: CDOM associated sink of superoxide in coastal waters. Environ. Sci. Technol. 34 (6), 1043–1048.
Greenstock, C.L., Ruddock, G.W., 1976. Determination of superoxide (O_2^-) radical anion reaction rates using pulse radiolysis. Int. J. Radiat. Phys. Chem. 8 (3), 367–369.
Grivennikova, V.G., Vinogradov, A.D., 2006. Generation of superoxide by the mitochondrial complex I. BBA Bioenergy 1757 (5-6), 553–561.
Guo, Y., Zhan, J., Yu, G., Wang, Y., 2021a. Evaluation of the concentration and contribution of superoxide radical for micropollutant abatement during ozonation. Water. Res. 194, 116927.
Guo, Y., Zhang, Y., Yu, G., Wang, Y., 2021b. Revisiting the role of reactive oxygen species for pollutant abatement during catalytic ozonation: The probe approach versus the scavenger approach. Appl. Catal. B Environ. 280, 119418.
Hansard, S.P., Easter, H.D., Voelker, B.M., 2011. Rapid reaction of nanomolar Mn(II) with superoxide radical in seawater and simulated freshwater. Environ. Sci. Technol. 45 (7), 2811–2817.
Hansard, S.P., Vermilyea, A.W., Voelker, B.M., 2010. Measurements of superoxide radical concentration and decay kinetics in the Gulf of Alaska. Deep Sea Res. Pt. I 57 (9), 1111–1119.
Hassan, I., Pinto, S., Weisbecker, C., Attygalle, A.B., 2016. Competitive deprotonation and superoxide [$O_2^{\bullet}$] radical-anion adduct formation reactions of carboxamides under negative-ion atmospheric-pressure helium-plasma ionization (HePI) conditions. J. Am. Soc. Mass Spectrom. 27 (3), 394–401.
Hayyan, M., Hashim, M.A., AlNashef, I.M., 2016. Superoxide ion: generation and chemical implications. Chem. Rev. 116 (5), 3029–3085.
Heller, M.I., Croot, P.L., 2010. Superoxide decay kinetics in the southern ocean. Environ. Sci. Technol. 44 (1), 191–196.
Holroyd, R.A., Bielski, B.H., 1978. Photochemical generation of superoxide radicals in aqueous solutions. J. Am. Chem. Soc. 100 (18), 5796–5800.
Ilan, Y.A., Meisel, D., Czapski, G., 1974. The redox potential of the O_2–O_2^- system in aqueous media. Isr. J. Chem. 12 (4), 891–895.
Iuga, C., Campero, A., Vivier-Bunge, A., 2015. Antioxidant vs. prooxidant action of phenothiazine in a biological environment in the presence of hydroxyl and hydroperoxyl radicals: a quantum chemistry study. RSC. Adv. 5 (19), 14678–14689.
Javed, H., Metz, J., Eraslan, T.C., Mathieu, J., Wang, B., Wu, G., Tsai, A.-L., Wong, M.S., Alvarez, P.J.J., 2020. Discerning the relevance of superoxide in PFOA degradation. Environ. Sci. Technol. Lett. 7 (9), 653–658.
Jin, F., Leitich, J., von Sonntag, C., 1993. The superoxide radical reacts with tyrosine-derived phenoxyl radicals by addition rather than by electron transfer. J. Chem. Soc. Perk. T. (9), 1583–1588.
Johnson, R.A., Nidy, E.G., 1975. Superoxide chemistry. Convenient synthesis of dialkyl peroxides. J. Org. Chem. 40 (11), 1680–1681.
Jones, A.M., Garg, S., He, D., Pham, A.N., Waite, T.D., 2011. Superoxide-mediated formation and charging of silver nanoparticles. Environ. Sci. Technol. 45 (4), 1428–1434.
Joshi, R., 2017. Superoxide radical anion scavenging and dismutation by some Cu^{2+} and Mn^{2+} complexes: A pulse radiolysis study. Radiat. Phys. Chem. 139, 74–82.
Kappler, A., Bryce, C., Mansor, M., Lueder, U., Byrne, J.M., Swanner, E.D., 2021. An evolving view on biogeochemical cycling of iron. Nature Rev. Microbiol. 19 (6), 360–374.
Kelley, E.E., Khoo, N.K., Hundley, N.J., Malik, U.Z., Freeman, B.A., Tarpey, M.M., 2010. Hydrogen peroxide is the major oxidant product of xanthine oxidase. Free. Radical Bio. Med. 48 (4), 493–498.
Kettle, A.J., Sangster, D.F., Gebicki, J.M., Winterbourn, C.C., 1988. A pulse radiolysis investigation of the reactions of myeloperoxidase with superoxide and hydrogen peroxide. BBA-Protein Struct. Mol. Enzymol. 956 (1), 58–62.
Kirby, M.E., Bullen, J.C., Hanif, M.D., Heiba, H.F., Liu, F., Northover, G.H.R., Resongles, E., Weiss, D.J., 2020. Determining the effect of pH on iron oxidation kinetics in aquatic environments: exploring a fundamental chemical reaction to grasp the significant ecosystem implications of iron bioavailability. J. Chem. Educ. 97 (1), 215–220.
Klug, D., Rabani, J., Fridovich, I., 1972. A direct demonstration of the catalytic action of superoxide dismutase through the use of pulse radiolysis. J. Biol. Chem. 247 (15), 4839–4842.
Klug-Roth, D., Fridovich, I., Rabani, J., 1973. Pulse radiolytic investigations of superoxide catalyzed disproportionation. Mechanism for bovine superoxide dismutase. J. Am. Chem. Soc. 95 (9), 2786–2790.
Kobayashi, K., Hayashi, K., Sono, M., 1989. Effects of tryptophan and pH on the kinetics of superoxide radical binding to indoleamine 2, 3-dioxygenase studied by pulse radiolysis. J. Biol. Chem. 264 (26), 15280–15283.
Kobayashi, K., Miki, M., Tagawa, S., 1995. Pulse-radiolysis study of the reaction of nitric oxide with superoxide. J. Chem. Soc., Dalton Trans. (17), 2885–2889.
Koppenol, W.H., 2001. The Haber-Weiss cycle-70 years later. Redox. Rep. 6 (4), 229–234.
Land, E.J., Navaratnam, S., Parsons, B.J., Phillips, G.O., 2010. Primary processes in the photochemistry of aqueous sulfacetamide—A laser flash-photolysis and pulse radiolysis study. Photochem. Photobiol. 35 (5), 637–642.
Learman, D.R., Voelker, B.M., Vazquez-Rodriguez, A.I., Hansel, C.M., 2011. Formation of manganese oxides by bacterially generated superoxide. Nat. Geosci. 4 (2), 95–98.
Lee, S.H., Jun, B.-H., 2019. Silver nanoparticles: synthesis and application for nanomedicine. Int J. Mol. Sci. 20 (4), 865.
Li, X., Liu, L., Liu, T., Yuan, T., Zhang, W., Li, F., Zhou, S., Li, Y., 2013. Electron transfer capacity dependence of quinone-mediated Fe(III) reduction and current generation by Klebsiella pneumoniae L17. Chemosphere 92 (2), 218–224.
Li, Y., Suleimanov, Y.V., Green, W.H., Guo, H., 2014. Quantum rate coefficients and kinetic isotope effect for the reaction Cl+ CH_4→ HCl+ CH_3 from ring polymer molecular dynamics. J. Phys. Chem. A 118 (11), 1989–1996.
Liang, S., Zheng, W., Zhu, L., Duan, W., Wei, C., Feng, C., 2019. One-step treatment of phosphite-laden wastewater: a single electrochemical reactor integrating superoxide radical-induced oxidation and electrocoagulation. Environ. Sci. Technol. 53 (9), 5328–5336.
Liou, S.-Y., Dodd, M.C., 2021. Evaluation of hydroxyl radical and reactive chlorine species generation from the superoxide/hypochlorous acid reaction as the basis for a novel advanced oxidation process. Water. Res. 200, 117142.
Liu, T., Niu, X., Shi, L., Zhu, X., Zhao, H., Lana, M., 2015. Electrocatalytic analysis of superoxide anion radical using nitrogen-doped graphene supported Prussian Blue as a biomimetic superoxide dismutase. Electrochim. Acta 176, 1280–1287.
Lokesh, B.R., Cunningham, M.L., 1986. Further studies on the formation of oxygen radicals by potassium superoxide in aqueous medium for biochemical investigations. Toxicol. Lett. 34 (1), 75–84.
Lu, X., Zhou, X., Qiu, W., Wang, Z., Wang, Y., Zhang, H., Yu, J., Wang, D., Gu, J., Ma, J., 2022. Kinetics and mechanism of the reaction of hydrogen peroxide with

hypochlorous acid: Implication on electrochemical water treatment. J .Hazard. Mater. 438, 129420.
Luo, Z., Spinney, R., Wei, Z., Hu, W.-P., Villamena, F.A., Song, W., Dionysiou, D.D., Xiao, R., 2021a. Reevaluation of the reactivity of superoxide radicals with a sulfonamide antibiotic, sulfacetamide: An experimental and theoretical study. ACS EST Water 1 (11), 2339–2347.
Luo, Z., Tseng, M.-Y., Minakata, D., Bai, L., Hu, W.-P., Song, W., Wei, Z., Spinney, R., Dionysiou, D.D., Xiao, R., 2021b. Mechanistic insight into superoxide radical-mediated degradation of carbon tetrachloride in aqueous solution: An in situ spectroscopic and computational study. Chem. Eng. J. 410, 128181.
Ma, J., Minakata, D., O'Shea, K., Bai, L., Dionysiou, D.D., Spinney, R., Xiao, R., Wei, Z., 2021. Determination and environmental implications of aqueous-phase rate constants in radical reactions. Water. Res. 190, 116746.
Ma, J., Nie, J., Zhou, H., Wang, H., Lian, L., Yan, S., Song, W., 2020. Kinetic consideration of photochemical formation and decay of superoxide radical in dissolved organic matter solutions. Environ. Sci. Technol. 54 (6), 3199–3208.
Ma, J., Zhou, H., Yan, S., Song, W., 2019. Kinetics studies and mechanistic considerations on the reactions of superoxide radical ions with dissolved organic matter. Water. Res. 149, 56–64.
Maeda, H., Yamamoto, K., Nomura, Y., Kohno, I., Hafsi, L., Ueda, N., Yoshida, S., Fukuda, M., Fukuyasu, Y., Yamauchi, Y., 2005. A design of fluorescent probes for superoxide based on a nonredox mechanism. J. Am. Chem. Soc. 127 (1), 68–69.
Marklund, S., 1976. Spectrophotometric study of spontaneous disproportionation of superoxide anion radical and sensitive direct assay for superoxide dismutase. J. Biol. Chem. 251 (23), 7504–7507.
Mayer, J.M., 2011. Understanding hydrogen atom transfer: from bond strengths to Marcus theory. Acc. Chem. Res. 44 (1), 36–46.
McDonald, R.N., Chowdhury, A.K., 1985. Gas-phase ion-molecule reactions of dioxygen anion radical (O_2^-). J. Am. Chem. Soc. 107 (14), 4123–4128.
McDowell, M.S., Bakac, A., Espenson, J.H., 1983. A convenient route to superoxide ion in aqueous solution. Inorg. Chem. 22 (5), 847–848.
McNeill, K., Canonica, S., 2016. Triplet state dissolved organic matter in aquatic photochemistry: reaction mechanisms, substrate scope, and photophysical properties. Environ. Sci. Proc Imp. 18 (11), 1381–1399.
Medinas, D.B., Cerchiaro, G., Trindade, D.F., Augusto, O., 2007. The carbonate radical and related oxidants derived from bicarbonate buffer. IUBMB Life 59 (4-5), 255–262.
Merritt, M.V., Sawyer, D.T., 1970. Electrochemical studies of the reactivity of superoxide ion with several alkyl halides in dimethyl sulfoxide. J. Org. Chem. 35 (7), 2157–2159.
Mesároš, Š., Vaňková, Ž., Mesárošová, A., Tomčík, P., Grunfeld, S., 1998. Electrochemical determination of superoxide and nitric oxide generated from biological samples. Bioelectroch. Bioener. 46 (1), 33–37.
Mitsuta, K., Mizuta, Y., Kohno, M., Hiramatsu, M., Mori, A., 1990. The application of ESR spin-trapping technique to the evaluation of SOD-like activity of biological substances. B. Chem. Soc. Jpn. 63 (1), 187–191.
Morones, J.R., Elechiguerra, J.L., Camacho, A., Holt, K., Kouri, J.B., Ramírez, J.T., Yacaman, M.J., 2005. The bactericidal effect of silver nanoparticles. Nanotechnology 16 (10), 2346.
Muhammad, H., Hanif, M., Tahiri, I.A., Versiani, M.A., Shah, F., Khaliq, O., Ali, S.T., Ahmed, S., 2018. Electrochemical behavior of superoxide anion radical towards quinones: a mechanistic approach. Res. Chem. Intermediat. 44 (10), 6387–6400.
Mukherjee, T., 1987. One-electron reduction of juglone (5-hydroxy-1,4-naphthoquinone): A pulse radiolysis study. Int. J. Radiat. Appl. Instrum. Part C 29 (6), 455–462.
Nagy, P., Kettle, A.J., Winterbourn, C.C., 2009. Superoxide-mediated formation of tyrosine hydroperoxides and methionine sulfoxide in peptides through radical addition and intramolecular oxygen transfer. J. Biol. Chem. 284 (22), 14723–14733.
Nanni Jr, E.J., Sawyer, D.T, 1980. Superoxide-ion oxidation of hydrophenazines, reduced flavins, hydroxylamine, and related substrates via hydrogen-atom transfer. J. Am. Chem. Soc. 102 (25), 7591–7593.
NIST, N., 2002. NIST solution kinetics database on the web. NIST Standard Ref. Datab. 40.
Nolte, T.M., Peijnenburg, W.J., 2018. Use of quantum-chemical descriptors to analyse reaction rate constants between organic chemicals and superoxide/hydroperoxyl ($O_2^{\bullet-}$/$HO_2^{\bullet}$). Free. Radical Res. 52 (10), 1118–1131.
Olean-Oliveira, A., Pacheco, J.C., Seraphim, P.M., Teixeira, M.F., 2019. Synergistic effect of reduced graphene oxide/azo-polymer layers on electrochemical performance and application as nonenzymatic chemiresistor sensors for detecting superoxide anion radicals. Electroanal. Chem. 852, 113520.
Ono, Y., Matsumura, T., Kitajima, N., Fukuzumi, S., 1977. Formation of superoxide ion during the decomposition of hydrogen peroxide on supported metals. J. Phys. Chem. 81 (13), 1307–1311.
Partridge, H., Bauschlicher, C.W., Sodupe, M., Langhoff, S.R., 1992. Theoretical determination of the alkali-metal superoxide bond energies. Chem. Phys. Lett. 195 (2), 200–206.
Pasternack, R.F., Halliwell, B., 1979. Superoxide dismutase activities of an iron porphyrin and other iron complexes. J. Am. Chem. Soc. 101 (4), 1026–1031.
Peover, M., White, B., 1966. Electrolytic reduction of oxygen in aprotic solvents: the superoxide ion. Electrochim. Acta 11 (8), 1061–1067.
Petasne, R.G., Zika, R.G., 1987. Fate of superoxide in coastal sea water. Nature 325 (6104), 516–518.
Pietta, P.-G., 2000. Flavonoids as antioxidants. J. Nat. Prod. 63 (7), 1035–1042.
Prasad, A.K., Mishra, P.C., 2015. Mechanism of action of sulforaphane as a superoxide radical anion and hydrogen peroxide scavenger by double hydrogen transfer: A model for Iron superoxide dismutase. J. Phys. Chem. B 119 (25), 7825–7836.
Privat, C., Trevin, S., Bedioui, F., Devynck, J., 1997. Direct electrochemical characterization of superoxide anion production and its reactivity toward nitric oxide in solution. Electroanal. Chem. 436 (1-2), 261–265.
Roberts Jr, J.L., Calderwood, T.S., Sawyer, D.T, 1983. Oxygenation by superoxide ion of tetrachloromethane, trichlorofluoromethane, trichloromethane, p, p'-DDT and related trichloromethyl substrates ($RCCl_3$) in aprotic solvents. J. Am. Chem. Soc. 105 (26), 7691–7696.
Rose, A.L., Waite, T.D., 2005. Reduction of organically complexed ferric Iron by superoxide in a simulated natural water. Environ. Sci. Technol. 39 (8), 2645–2650.
Rose, A.L., Waite, T.D., 2006. Role of superoxide in the photochemical reduction of iron in seawater. Geochim. Cosmochim. Ac. 70 (15), 3869–3882.
Rotilio, G., Bray, R.C., Fielden, E.M., 1972. A pulse radiolysis study of superoxide dismutase. BBA-Enzymol. 268 (2), 605–609.
Rush, J.D., Zhao, Z., Bielski, B.H., 1996. Reaction of ferrate (VI)/ferrate (V) with hydrogen peroxide and superoxide anion-a stopped-flow and premix pulse radiolysis study. Free. Radical Res. 24 (3), 187–198.
Sacramento, J.J.D., Goldberg, D.P., 2019. The hydrogen atom transfer reactivity of a porphyrinoid cobalt superoxide complex. Chem. Commun. 55 (7), 913–916.
Sawada, Y., Yamazaki, I., 1973. One-electron transfer reactions in biochemical systems. VIII. Kinetic study of superoxide dismutase. BBA-Enzymol 327 (2), 257–265.
Sawyer, D.T., 1991. Oxygen chemistry. Oxford university press.
Sawyer, D.T., Calderwood, T.S., Johlman, C.L., Wilkins, C.L., 1985. Oxidation by superoxide ion of catechols, ascorbic acid, dihydrophenazine, and reduced flavins to their respective anion radicals. A common mechanism via a combined proton-hydrogen atom transfer. J. Org. Chem. 50 (9), 1409–1412.
Sawyer, D.T., Chiericato Jr, G., Tsuchiya, T, 1982. Oxidation of ascorbic acid and dehydroascorbic acid by superoxide ion in aprotic media. J. Am. Chem. Soc. 104 (23), 6273–6278.
Sawyer, D.T., Gibian, M.J., Morrison, M.M., Seo, E.T., 1978. On the chemical reactivity of superoxide ion. J. Am. Chem. Soc. 100 (2), 627–628.
Sawyer, D.T., Roberts, J.L., 1966. Electrochemistry of oxygen and superoxide ion in dimethylsulfoxide at platinum, gold and mercury electrodes. J. Electroanal. Chem. 12 (2), 90–101.
Sawyer, D.T., Valentine, J.S., 1981. How super is superoxide? Acc. Chem. Res. 14 (12), 393–400.
Sawyer, D.T., Yamaguchi, K., Calderwood, T.S., 2018. Electrochemical generation of superoxide ion and other. Handbook Methods Oxygen Radical Res. 65.
Scott, D.T., McKnight, D.M., Blunt-Harris, E.L., Kolesar, S.E., Lovley, D.R., 1998. Quinone moieties act as electron acceptors in the reduction of humic substances by humics-reducing microorganisms. Environ. Sci. Technol. 32 (19), 2984–2989.
Shaked, Y., Harris, R., Klein-Kedem, N., 2010. Hydrogen peroxide photocycling in the Gulf of Aqaba, Red Sea. Environ. Sci. Technol. 44 (9), 3238–3244.
Sheng, Y., Abreu, I.A., Cabelli, D.E., Maroney, M.J., Miller, A.-F., Teixeira, M., Valentine, J.S., 2014. Superoxide dismutases and superoxide reductases. Chem. Rev. 114 (7), 3854–3918.
Sivakumar, P., Prabhakar, P., Doble, M., 2011. Synthesis, antioxidant evaluation, and quantitative structure–activity relationship studies of chalcones. Med. Chem. Res. 20 (4), 482–492.
Smith, B.A., Teel, A.L., Watts, R.J., 2004. Identification of the reactive oxygen species responsible for carbon tetrachloride degradation in modified Fenton's systems. Environ. Sci. Technol. 38 (20), 5465–5469.
Stemmler, E.A., Diener, J.L., Swift, J.A., 1994. Gas-phase reactions of O_2^- with alkyl and aryl esters of benzenedicarboxylic acids. J. Am. Soc. Mass Spectrom. 5 (11), 990–1000.
Stewart, J.J., 2013. Optimization of parameters for semiempirical methods VI: more modifications to the NDDO approximations and re-optimization of parameters. J . Mol. Model 19, 1–32.
Stoin, U., Shames, A.I., Malka, I., Bar, I., Sasson, Y., 2013. In situ generation of superoxide anion radical in aqueous medium under ambient conditions. Chemphyschem. 14 (18), 4158–4164.
Sutherland, K.M., Wankel, S.D., Hansel, C.M., 2020. Dark biological superoxide production as a significant flux and sink of marine dissolved oxygen. P. Natl. Acad. Sci. USA 117 (7), 3433–3439.
Teel, A.L., Watts, R.J., 2002. Degradation of carbon tetrachloride by modified Fenton's reagent. J. Hazard. Mater. 94 (2), 179–189.
Valentine, J.S., Curtis, A.B., 1975. Convenient preparation of solutions of superoxide anion and the reaction of superoxide anion with a copper (II) complex. J. Am. Chem. Soc. 97 (1), 224–226.
Voelker, B.M., Sedlak, D.L., Zafiriou, O.C., 2000. Chemistry of superoxide radical in seawater: reactions with organic Cu complexes. Environ. Sci. Technol. 34 (6), 1036–1042.
Waddell, W.J., 1956. A simple ultraviolet spectrophotometric method for the determination of protein. J. Lab. Clin. Med. 48 (2), 311–314.
Wang, D., Zhao, L., Ma, H., Zhang, H., Guo, L.-H., 2017. Quantitative analysis of reactive oxygen species photogenerated on metal oxide nanoparticles and their bacteria toxicity: the role of superoxide radicals. Environ. Sci. Technol. 51 (17), 10137–10145.
Wang, Q., Zhou, H., Liu, X., Li, T., Jiang, C., Song, W., Chen, W., 2018a. Facet-dependent generation of superoxide radical anions by ZnO nanomaterials under simulated solar light. Environ. Sci. Nano 5 (12), 2864–2875.
Wang, Y., Li, F., Song, J., Xiao, R., Luo, L., Yang, Z., Chai, L., 2018b. Stabilization of Cd-, Pb-, Cu-and Zn-contaminated calcareous agricultural soil using red mud: a field experiment. Environ. Geochem. Health 40, 2143–2153.
Watts, R.J., Bottenberg, B.C., Hess, T.F., Jensen, M.D., Teel, A.L., 1999. Role of reductants in the enhanced desorption and transformation of chloroaliphatic

compounds by modified Fenton's reactions. Environ. Sci. Technol. 33 (19), 3432–3437.
Watts, R.J., Stanton, P.C., Howsawkeng, J., Teel, A.L., 2002. Mineralization of a sorbed polycyclic aromatic hydrocarbon in two soils using catalyzed hydrogen peroxide. Water. Res. 36 (17), 4283–4292.
Wei, Y., Dang, X., Hu, S., 2004. Electrochemical properties of superoxide ion in aprotic media. Russ. J. Electrochem. 40, 400–404.
Wei, Y., Wu, K., Wu, Y., Hu, S., 2003. Electrochemical characterization of a new system for detection of superoxide ion in alkaline solution. Electrochem. Commun. 5 (9), 819–824.
Wei-Haas, M.L., Hageman, K.J., Chin, Y.-P., 2014. Partitioning of polybrominated diphenyl ethers to dissolved organic matter isolated from arctic surface waters. Environ. Sci. Technol. 48 (9), 4852–4859.
Westheimer, F.H., 1961. The magnitude of the primary kinetic isotope effect for compounds of hydrogen and deuterium. Chem. Rev. 61 (3), 265–273.
Wilshire, J., Sawyer, D.T., 1979. Redox chemistry of dioxygen species. Acc. Chem. Res. 12 (3), 105–110.
Wojnárovits, L., Takács, E., 2019. Rate constants of sulfate radical anion reactions with organic molecules: A review. Chemosphere 220, 1014–1032.
Wood, P.M., 1974. The redox potential of the system oxygen—superoxide. FEBS Lett. 44 (1), 22–24.
Wuttig, K., Heller, M.I., Croot, P.L., 2013a. Pathways of superoxide (O_2^-) decay in the eastern tropical north atlantic. Environ. Sci. Technol. 47 (18), 10249–10256.
Wuttig, K., Heller, M.I., Croot, P.L., 2013b. Reactivity of inorganic Mn and Mn desferrioxamine B with O_2, O_2^-, and H_2O_2 in Seawater. Environ. Sci. Technol. 47 (18), 10257–10265.
Xia, C., Qu, S., Bhattacharjee, L., Lim, X.E., Yang, H., Liu, J., 2022. Degradation of perfluoroalkyl substances using UV/Fe0 system with and without the presence of oxygen. Environ. Technol. 1–12.
Xiao, R., Ye, T., Wei, Z., Luo, S., Yang, Z., Spinney, R., 2015. Quantitative structure–activity relationship (QSAR) for the oxidation of trace organic contaminants by sulfate radical. Environ. Sci. Technol. 49 (22), 13394–13402.
Xiao, Y., Carena, L., Näsi, M.-T., Vähätalo, A.V., 2020. Superoxide-driven autocatalytic dark production of hydroxyl radicals in the presence of complexes of natural dissolved organic matter and iron. Water. Res. 177, 115782.
Xu, X., Wang, J., Chen, T., Yang, N., Wang, S., Ding, X., 2021. Deep insight into ROS mediated direct and hydroxylated dichlorination process for efficient photocatalytic sodium pentachlorophenate mineralization. Appl. Catal. B-Environ. 296, 120352.
Yamagami, C., Akamatsu, M., Motohashi, N., Hamada, S., Tanahashi, T., 2005. Quantitative structure–activity relationship studies for antioxidant hydroxybenzalacetones by quantum chemical-and 3-D-QSAR (CoMFA) analyses. Bioorg. Med. Chem. Lett. 15 (11), 2845–2850.
Ye, T., Wei, Z., Spinney, R., Tang, C.-J., Luo, S., Xiao, R., Dionysiou, D.D., 2017. Chemical structure-based predictive model for the oxidation of trace organic contaminants by sulfate radical. Water. Res. 116, 106–115.
Yeager, E., 1984. Electrocatalysts for O_2 reduction. Electrochim. Acta 29 (11), 1527–1537.
Yu, X.-Y., 2004. Critical evaluation of rate constants and equilibrium constants of hydrogen peroxide photolysis in acidic aqueous solutions containing chloride ions. J. Phys. Chem. Ref. Data 33 (3), 747–763.
Zafiriou, O., 1990. Chemistry of superoxide ion-radical (O_2^-) in seawater. I. pKasw* (HOO) and uncatalyzed dismutation kinetics studied by pulse radiolysis. Mar. Chem. 30, 31–43.
Zhang, B.-T., Zhang, Y., Teng, Y., Fan, M., 2015. Sulfate radical and its application in decontamination technologies. Crit. Rev. Env. Sci. Tec. 45 (16), 1756–1800.
Zhang, Y., Li, J., Bai, J., Li, L., Xia, L., Chen, S., Zhou, B., 2017. Dramatic enhancement of organics degradation and electricity generation via strengthening superoxide radical by using a novel 3D AQS/PPy-GF cathode. Water. Res. 125, 259–269.